THE UNIVERSITY OF MANITOBA

A STUDY OF PROTON INDUCED X-RAY FLUORESCENCE AND MAGNETIC REGENERATION, THE CONSTRUCTION OF A HELICAL WIRE CHAMBER AND A MECHANISM FOR DIPROTON PRODUCTION IN THE SUN

by

C. P. RANDELL

A THESIS

SUBMITTED TO THE FACULTY OF GRADUATE STUDIES

IN PARTIAL FULFILMENT OF THE REQUIREMENTS FOR THE DEGREE

OF MASTER OF SCIENCE

DEPARTMENT OF PHYSICS

WINNIPEG, MANITOBA

May 1976

THE UNIVERSITY OF MANITOBA LIBRARIES

"A STUDY OF PROTON INDUCED X-RAY FLUORESCENCE AND MAGNETIC REGENERATION, THE CONSTRUCTION OF A HELICAL WIRE CHAMBER AND A MECHANISM FOR DIPROTON PRODUCTION IN THE SUN"

by

C. P. RANDELL

A dissertation submitted to the Faculty of Graduate Studies of the University of Manitoba in partial fulfillment of the requirements of the degree of

MASTER OF SCIENCE

© 1976

Permission has been granted to the LIBRARY OF THE UNIVERSITY OF MANITOBA to lend or sell copies of this dissertation, to the NATIONAL LIBRARY OF CANADA to microfilm this dissertation and to lend or sell copies of the film, and UNIVERSITY MICROFILMS to publish an abstract of this dissertation.

The author reserves other publication rights, and neither the dissertation nor extensive extracts from it may be printed or otherwise reproduced without the author's written permission.

ABSTRACT

The details of 4 separate projects are reported and the results obtained prior to May 1976 are described. The first chapter gives the progress made towards the development of an on-line trace element analysis system using X-ray fluorescence excited by 20 - 50 MeV protons. A study of K shell X-rays from heavy elements has given results for the K_β:K_α and K_{α_2}:K_{α_1} ratios and the K shell ionization cross section. The nature of a satellite peak on the high energy side of K_α and K_β groups is identified and preliminary results for the preparation of environmental samples are outlined.

The second chapter gives details of a program written to design a magnetic regenerator and to determine the extent to which the proton orbits in the cyclotron can be distorted by this regenerator and an electrostatic peeler. An increase in turn-to-turn separation from 0.2 mm to 4 mm is obtained. This should be sufficient to allow extraction of a proton beam using an electrostatic deflector which would enable the acceleration of positive rather than negative ions, resulting in increased beam intensity.

The third chapter describes the progress up to May 1976 in the design, construction and testing of a multiwire proportional counter with delay lines incorporated into both cathode and anode planes. The basis for the design has been the chamber described by Lee (1973, 1974).

The final chapter outlines the results from a study of diproton production in the reaction $^3He(^3He, 2_p)^4He$. The mechanism for this reaction was determined below the Coulomb barrier and the implication of our results along with those of Slobodrian (1975) has been considered in the hydrogen burning cycle.

ACKNOWLEDGEMENTS

I wish to acknowledge the supervision of Dr. J.S.C. McKee throughout these projects, and that of Dr. S. Oh in the design of the magnetic regenerator. I would also like to thank all the cyclotron staff and graduate students for their help in each of these projects.

A COMMENT ON THE STRUCTURE OF THIS THESIS

This thesis is divided into 4 Chapters describing 4 separate projects I have undertaken with the cyclotron group at the University of Manitoba during the period between September 1974 and April 1976. The cyclotron group is supported by an A.E.C.B. grant, the machine is a sector focused cyclotron which is capable of producing proton beams in the energy range 20 - 50 MeV with typical intensities between 1 and 5 μA.

A recently installed axial injection system, see R.A. Batten (1976), injects a beam of negative hydrogen ions into the centre of the cyclotron at 11 keV. The ions are deflected into the median plane by an electrostatic mirror and accelerated by a 28 keV rf voltage. Extraction is achieved by stripping the two electrons from the negative hydrogen ions using a thin Aluminium foil, the magnetic force reverses, sweeping the beam out of the cyclotron field. Changing the stripping foil radius and angle and the use of a small exterior magnetic field (the combination magnet) allows extraction of proton beams varying from 20 to 50 MeV (see Fig. 1). The single main beam line serves 5 separate experimental lines by means of a switching magnet.

The first project involved the study of proton induced X-ray fluorescence, measuring production cross sections and intensity ratios of various X-ray components for heavy elements. This work was carried out with the aim of establishing an on-line trace element analysis system with a particular interest in heavy elements since it is felt that the use of higher proton energies than those used previously leads to several advantages in obtaining accurate values for heavy element concentrations in the order of 1 - 10 ppm. This topic forms the major part of my thesis, the research carried out up to April 1st, 1976 being described in Chapter I.

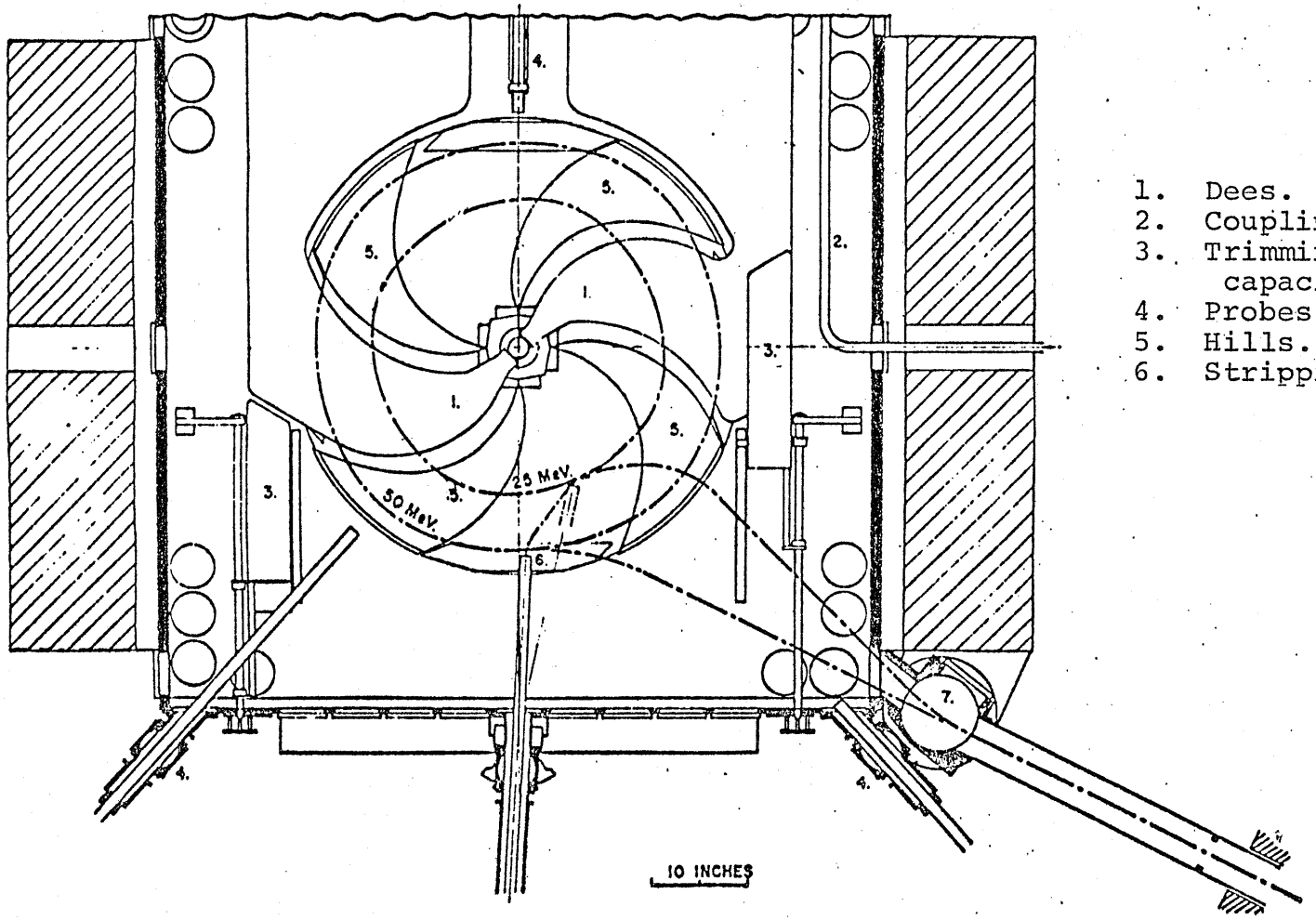

Figure 1. The interior of the cyclotron.

The second project was a design study of a magnetic regerator which would enable the acceleration of protons rather than negative hydrogen ions in the cyclotron. Since the production rate of negative ions in a plasma is at least one order of magnitude below the rate for proton production a considerable increase in beam can be gained with a high extraction efficiency. However the turn-to-turn separation of orbits within the Manitoba cyclotron is only 0.2 mm which is too small for the normal extraction method of positive ions, that is to position an electrostatic deflector such that the protons are swept from the cyclotron field. With so small a turn-to-turn separation the beam would be lost into the deflector.

A magnetic regenerator and electrostatic peeler make up a system which perturbs the field in such a way as to distort the proton orbit, increasing the turn-to-turn separation sufficiently to enable the use of an electrostatic deflector with a high extraction efficiency. A program was written to design a suitable regenerator and to determine the maximum turn-to-turn separation that could be achieved. A summary of the program is given in Chapter II,the program is listed in Appendix II.

In the spring of 1975 a third project was undertaken, this was to design and construct a muliwire proportional counter using delay line readout in both anode and cathode planes as described by D. Lee (1973, 1974). This chamber was designed with the view to its use in a radiative captive experiment which is under preliminary study at the present time. In this project, with the assistance of A. Hathaway, a first chamber was built during the summer but proved unsuccessful. A second has recently been built and has given good results. Its basic principles, design features and the results of recent tests are described in Chapter III.

Finally during my first winter in Manitoba a theoretical project was undertaken to determine the effect of diproton production on the hydrogen burning cycle. Recent experimental results (Slobodrian 1975) have indicated that there exists a substantially higher branching ratio for $^3He + ^3He \rightarrow ^4He + d + e^- + \nu$ over $^3He + ^3He \rightarrow ^4He + p + p$ than expected, our calculations suggest that both these reactions proceed via an intermediate anti-bound state of two protons commonly called the diproton or ^2He for reaction energies below the Coulomb barrier. The effect of this high branching ratio on the equilibrium calculation for a main sequence star with a non-convective core (particularly the sun) has been considered. Results show that this would not help in an explanation of "the solar neutrino problem". The papers published on this topic make up Chapter IV.

CONTENTS

		Page
ABSTRACT		ii
ACKNOWLEDGEMENTS		iii
A COMMENT ON THE STRUCTURE OF THIS THESIS		iv
CHAPTER I.	PROTON INDUCED X-RAY ANALYSIS OF HEAVY ELEMENTS AS AN ENVIRONMENTAL PROBE	1
1.	INTRODUCTION	2
2.	X-RAY FLUORESCENCE - THEORY	4
2.1	Atomic Ionization	4
2.2	De-Excitation of Ionized Atoms	5
2.3	Allowed Transitions	6
3.	X-RAY FLUORESCENCE - ITS USE IN A TRACE ELEMENT ANALYSIS SYSTEM	9
3.1	Proton Induced X-Ray Emission (P.I.X.E.) in Trace Element Analysis	10
3.2	Target Preparation	12
3.3	Use of 40 MeV Protons in a Trace Element Analysis System	16
4.	EXPERIMENTAL PROCEDURE	18
4.1	Scattering Chamber	18
4.2	Ge(Li) Detector	18
4.3	Beam Monitoring	21
4.4	Data Taking and Analysis	21
5.	RESULTS	24
5.1	K_β:K_α, K_{α_2}:K_{α_1} Ratios	24
5.2	Ionization Cross Sections	27
6.	THE IDENTIFICATION OF THE NATURE OF A SATELLITE PEAK	29
7.	PRELIMINARY INVESTIGATION FOR THE ESTABLISHMENT OF A TRACE ELEMENT ANALYSIS SYSTEM	34
8.	CONCLUSION	39

Page

CHAPTER II. THE DESIGN OF A MAGNETIC REGENERATOR WHICH WILL ENABLE THE ACCELERATION AND EXTRACTION OF POSITIVE IONS FROM THE MANITOBA CYCLOTRON 41

1. POSITIVE ION ACCELERATION 42

2. OUTLINE OF PROGRAM 45

2.1 Field Mapping and Proton Deflection 45
2.2 Orbit Calculation 50

3. CONCLUSION 54

CHAPTER III. A MULTIWIRE PROPORTIONAL COUNTER WITH DELAY LINE READOUT 55

1. INTRODUCTION 56

2. PRINCIPLES 59

2.1 Multi-Wire Proportional Counters 59
2.2 The Cathode Delay Line 60
2.3 The Anode Delay Line 66

3. CONSTRUCTION DETAILS 68

4. TESTING OF THE CHAMBER 72

5. CONCLUSION 77

CHAPTER IV. A MECHANISM FOR DIPROTON PRODUCTION IN THE SUN AND ITS EFFECT ON THE HYDROGEN BURNING CYCLE 78

1. INTRODUCTION 79

2. REPRINTS 80

2.1 Neutron Tunnelling as a Mechanism for Diproton Production 80
2.2 Diproton Production, and its Influence on the Hydrogen Burning Cycle 82

BIBLIOGRAPHY 87

APPENDIX I. 90

1. X-RAY AND GAMMA RAY INTERACTION WITH MATTER 90

2. COMPTON BACKGROUND IN SOLID STATE DETECTORS 90

Page

APPENDIX II. 93

1. FIELD MAPPING AND PROTON DEFLECTION 94

2. ORBIT DEFLECTION 95

3. SUBPROGRAM: LINE 98

4. SUBPROGRAM: LINE2 99

5. SUBPROGRAM: MAGFLD 100

6. SUBPROGRAM: INTGRL 101

LIST OF FIGURES

Figure		Page
1.	The interior of the cyclotron	v
2.	Allowed transitions for singly ionized atom	7
3.	Mass absorption coefficient for X-rays in lead	13
4.	The experimental area at the Manitoba cyclotron	19
5.	The β-γ spectrometer	20
6.	Schematic diagram of experimental set up	22
7.	Typical spectra from lead, gold and tantalum	25
8.	Relative ionization cross sections for lead and gold	28
9.	Background spectrum from borax-graphite pellet	35
10.	Background spectrum from millipore filter	37
11.	Peeler-regenerator location in cyclotron	43
12.	Regenerator parameters used in program	47
13.	Deflection of proton orbit caused by regenerator	49
14.	Monofilar helical cathode and anode delay line	58
15.	Bifilar helical cathode	61
16.	Approximations made by sheaf helix model	63
17.	Impedance as a function of frequency for monofilar helix	64
18.	Impedance reduction factor	65
19.	Copper etched anode delay line	67
20.	Master copy used to make copper contacts for anode wires	69
21a.	Transmission of pulses down anode delay line	73
21b.	Transmission of pulse through cathode helix	73
22.	Electronics set up to test wire chamber	74

LIST OF TABLES

Table		Page
1.	K_β:K_α ratio	26
2.	$K_{\alpha 2}$:$K_{\alpha 1}$ ratio	26
3.	Field mapping and proton deflection	46
4.	Orbit deflection	51
5.	Parameters of proton orbit as the central region of the perturbing fields is passed	53

CHAPTER I

PROTON INDUCED X-RAY ANALYSIS OF HEAVY ELEMENTS AS AN ENVIRONMENTAL PROBE

INTRODUCTION

X-ray fluorescence is one of two de-excitation processes which follow the ionization of inner-shell electrons, the other being the emission of Auger electrons. The study of "characteristic X-rays" following ionization by heavy charged particles dates back 60 years. J. Chadwick (1912) observed this phenomenon by exposing elements to alpha particles emitted from a radioactive source. However, it is only in the last 15 to 20 years that a more thorough study has developed both theoretically and experimentally, the latter being encouraged by the recent development of solid state detectors with high efficiency and good resolution. In this time ionization cross sections have been measured for a wide range of elements induced by protons of energies up to 10 MeV, the results showing good agreement with theory. However for proton energies above 10 MeV results are scarce.

At the same time it has been realized that this phenomenon presents a powerful method for determining elemental concentrations within an unknown sample since the energy of the "characteristic" X-ray lines is a continuously varying function of Z. This technique is now a well established tool for trace element analysis of environmental, clinical and biological samples.

Proton energies commonly used for such a system are between 0.4 and 5 MeV using a Si(Li) detector to record the X-ray emission spectrum. The K X-ray series is normally used for elements in the range $15 < Z < 50$ and the L X-ray series for heavier elements (see Sec. 3).

Various authors have attempted to calculate the most suitable energies to gain the maximum possible sensitivity for specific elements.

Results are inconsistent. Folkmann (1974) suggests 1 - 10 MeV proton energies whereas Verba (1972) and Gordon (1972) suggests 10 - 40 MeV. The common use of low energies is probably due to the abundance of low energy accelerators rather than this being the optimum energy.

However there is one component in the X-ray background, the Compton scattering of gamma rays in the detector crystal (see Appendix I) which, it has been suggested, increases sufficiently to obscure the characteristic X-ray lines when the proton energy is increased from 3 to 40 MeV. A. Gervé and G. Schatz, in an invited paper to the Seventh Int. Conference on Cyclotrons and Their Applications (1975) states categorically that cyclotrons can find only limited application in ion-induced X-ray analysis and that there is no significant advantage in studying X-ray fluorescence at energies higher than a few MeV. W. Wolfli has expressed similar beliefs in a private communication.

Having obtained high resolution K X-ray spectra from lead following bombardment by 40 MeV protons, we have undertaken a study of the K X-ray emission spectra induced by 20 - 50 MeV protons, with a particular aim of establishing a trace element analysis system. With an increase in proton energy from 3 to 40 MeV the K shell ionization cross section increases by 3 orders of magnitude making possible the use of the K series for detection of heavy as well as light elements, the K series having considerable advantages in detecting trace elements over the L series, see Sec. 3.3.

2. X-RAY FLUORESCENCE - THEORY

2.1 Atomic Ionization

In the 60 years during which atomic ionization has been studied three formulations have been developed which now show good agreement with experimental observations. Two of these are "high energy" theories, that is they apply for projectile energies very much greater than the electron binding energies. These are the Born approximation (Henneberg, 1933; Merzbacher, 1958) and the impulse or binary encounter approximation (Gryzinski, 1965; Garcia, 1970). The third is applicable for low energies close to threshold, this is the impact parameter method (Bang, 1959). These theories are reviewed in detail by Garcia (1973).

The criterion given for the applicability of the Born approximation gives a quantitative interpretation of "high energy". This is,

$$\frac{zZe^2}{\hbar v} \gg 1$$

where z, Z are the charge of the projectile and target element and v is the relative velocity. This requires that in considering K shell ionization by proton impact the latter's energy E_p must fulfil the condition,

$$E_p/u_k \gg 24$$

where u_k is the K shell binding energy. This condition shows that the high energy formulations apply for protons with energy between 20 and 50 MeV.

Each formulation gives results which suggest that by scaling the ionization cross section σ_I by a factor u_x^2/Z^2 and plotting this function against the proton energy E_p scaled by $\frac{m_e}{m_p} \cdot \frac{1}{u_x}$ a single

universal curve is followed by the data from all target atoms, where m_e, m_p are the electron and proton mass, u_x the electron binding energy.

In Garcia's paper (Garcia, 1973) the data from a variety of experiments are compared with the two high energy formulations on a universal plot. The various experiments show a significant distribution, the two theoretical curves lying within this distribution.

We have measured the cross section for lead and gold and compared our results with those of F. Bodart (1975) which were obtained through bombardment of elements from Ti to Cu with protons of energies in the range 0.4 to 2.3 MeV, and those from G.A. Bissinger (1972) which were obtained by bombarding Ag with 2 to 30 MeV protons.

2.2 De-excitation of Ionized Atoms

Following ionization of an inner-shell electron de-excitation proceeds through the transition of an electron from a higher orbital to the vacancy shell with the emission of either an X-ray or an Auger electron.

X-ray emission is dominated by one photon electric dipole radiation, thus the transitions are severely restricted by selection rules. However, Auger electron emission proceeds through a repulsive interaction proportional to e^2/r. The selection rules are

$\Delta L = \Delta J = \Delta S = \Delta(\text{parity}) = 0$ but since the emitted electron can have any angular momentum the number of accessible final states has considerably fewer restrictions.

This results in an X-ray spectrum which is very simple in comparison with the Auger electron spectrum. For this reason the study of inner shell vacancy production has been predominantly through the measurement of X-ray fluorescence spectrum, despite the fact that for

$Z < 30$ there is a higher probability for Auger emission following K shell ionization.

In order to determine ionization cross sections σ_I through recording of X-ray spectrum it is necessary to know the relative probability for the two processes as a function of Z. The fluorescence yield ω is defined so that,

$$\sigma_I = \frac{\sigma_Z}{\omega} = \frac{\sigma_A}{1-\omega} \qquad (1)$$

where σ_Z is the X-ray production cross section and σ_A is the Auger electron cross section. The direct experimental determination of ω has only been possible with high uncertainties and the results of various experiments show large discrepancies. The results of Bambynek (1972) are often used in comparison of σ_Z with σ_I , also improved theoretical values are given by McGuire (1969) Kostroun (1971) and Walters (1971) and these may be used since they avoid the large uncertainties associated with experimentally determined values.

2.3 Allowed Transitions

The various components of the characteristic X-rays are formed into groups according to the particular shell in which the vacancy exists. Owing to the hyperfine splitting of the various atomic levels the different series are made up of several lines. Fig. 2 shows the allowed transitions following K, L, M shell ionization.

The energy of each component and its relative intensity have been the subject of many experiments. The energies of the major K and L components have been tabulated in a single table for all Z, see "Nucleonics Data sheet No. 1. Physical Constants" (1955). These values were largely obtained experimentally, the remainder being calculated by extrapolation using Moseley's Law.

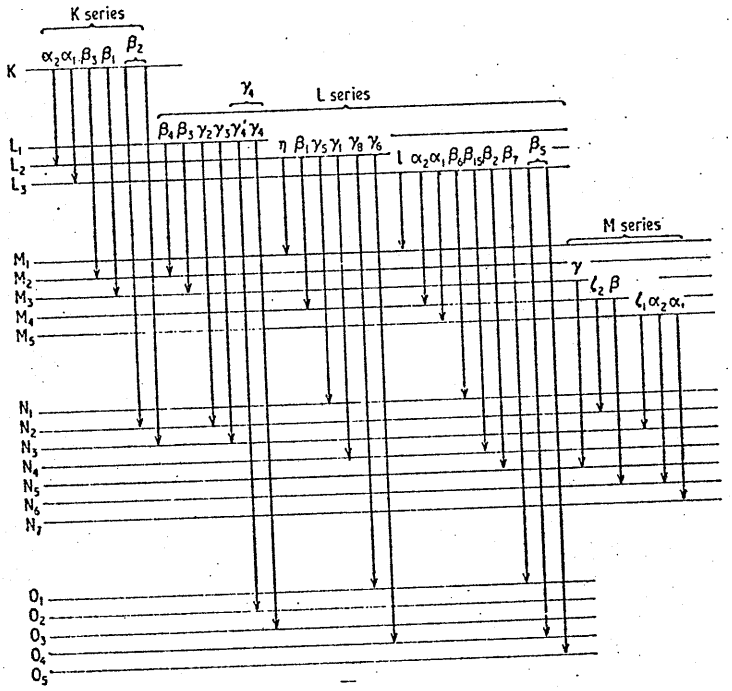

Figure 2. Energy level diagram for a singly ionized atom, from Dyson (1975). The diagram contains all the lines for which specific symbols are listed by Bearden (1967), except for a few weak quadrupole transitions. Many additional lines have been identified, especially in the heavier elements. Arabic subscripts for sub-shells (following Bambynek et al. 1972) are used.

There is considerable experimental variation in the values which have been obtained for the relative intensities of the components in each group. Nelson (1969) gives a comparison of theory and experiment for the $K_{\alpha_2}:K_{\alpha_1}$ ratio, both the experimental results and the various theoretical approaches show a variation in the order of 10%, however there is good agreement between the two. Middleman (1970) shows a comparison for the $K_\beta:K_\alpha^*$ ratio, however the theory (Scofield, 1969) is consistently high for all Z. We have measured values for both these ratios for 4 elements and have compared them with results obtained using other ionizing radiation, with a least squares fit carried by Rao (1972) to the data from 12 experiments, and with the theory of Scofield (1969).

---

*K_α is used to denote the sum of the components K_{α_1}, and K_{α_2}; similarly, K_β denotes the sum of K_{β_1}, K_{β_2} and K_{β_3}.

3. X-RAY FLUORESCENCE - ITS USE IN A TRACE ELEMENT ANALYSIS SYSTEM

X-ray fluorescence is now a well established tool for trace element analysis, its potential is apparent from the fact that the X-ray emission energies following inner-shell vacancy production are a continuously varying function of Z. Neglecting the effect of hyperfine splitting the X-ray energy, E_k, following K shell ionization is given by,

$$E_k = 13.6\ (Z^2-(Z-s)^2) \times 3/4 \quad \text{(eV)} \qquad (2)$$

where s is the screening factor. This is given a value of 5/16 for K shell ionization for all Z. This expression is approximate and could not be used in a trace element analysis system to identify the elements in an unknown sample, however, as mentioned in Sec. 2.3, the X-ray emission energies have been measured accurately (to 1eV) for most elements and a comprehensive tabulation of these results have been drawn up by Nucleonics (1955).

The development of solid state detectors has enabled this potential to be utilized, Si(Li) and Ge(Li) detectors are capable of handling high X-ray fluxes ($\sim$ 1,000 c.p.s.) with up to 100% efficiency producing high resolution spectra. Trace element analysis systems have been developed using this phenomenon induced by X-ray sources, electrons, protons and heavy ion beams. Intercomparisons of these techniques have been carried out (D.C. Camp, 1975). Generally X-ray fluorescence has the advantage of being a fast multi-element technique. However, its limit of sensitivity is no lower than the limit of other trace element analysis methods, 0.1 - 10 ppm being obtainable for $Z > 15$. It is not possible to use this technique for lighter elements since solid state detectors are not capable of resolving the K X-rays from neighbouring elements.

3.1 Proton Induced X-ray Emission (P.I.X.E.) in Trace Element Analysis

P.I.X.E. has become one of the most successful fluorescence techniques. The normal set up is for an environmental sample to be orientated at 45° to the incident beam, typical proton energies being 0.5 - 5 MeV. The X-ray spectrum is recorded using a Si(Li) detector set at an angle of 90° to the beam. The K X-ray series is normally used to determine concentrations of elements with $15 < Z < 50$, however, because of the rapid fall off of ionization cross section with Z the K series for heavier elements is obscured by the X-ray background. Due to the considerably higher probability for L shell ionization it is possible to use the L series to detect these elements. It should be noted that this presents some problems due to the considerably more complex form of the L series, to the very small separation of neighbouring elements and to the fact that they overlap the energy region of the K series from lighter elements.

The fractional concentration of a particular element ρ_z can be determined for thin targets from the relationship,

$$\rho_z = \frac{N_z}{N_p \sigma_z} \cdot \frac{4\pi}{\Omega} \cdot \frac{1}{\varepsilon} \cdot \frac{m_z t}{M_s} \qquad (3)$$

where N_z - denotes the number of photons from element Z

σ_z - the X-ray production cross section of element Z

N_p - the number of protons

ε - the efficiency of the detector

Ω - the solid angle subtended by the detector

M_s - the mass of the sample

M_z - the atomic mass of element Z

t - the thickness of sample

A precise knowledge of each parameter is necessary to arrive at an accurate value for ρ_Z.

The spectrum obtained from an environmental sample can consist of a complex distribution of overlapping peaks on a non-linear background. The problem of unfolding the peaks from the background to obtain accurate values for N_Z has been overcome by the development of appropriate peak fitting programs. There are however several problems which are not readily solved in this way. The complex form of the K and L series and the fact that they overlap below ~16 keV causes problems in peak identification. The lower intensity components of both series may not be resolved above background for very low concentrations or when a high concentration of a neighbouring element is present. These problems can only be overcome with an accurate knowledge of the relative intensities of the components of the K and L series.

Having unfolded and identified the peaks in the spectrum from environmental sample the cross section σ_Z is required in order to determine the various elemental concentrations. This is related to the ionizing cross section σ_I by the fluorescence yield, see Sec. 2.2.

As mentioned in Sec. 2.1 a comparison of experimental results drawn up by Garcia (1973) shows considerable variation when compared with the universal curve suggested by theory, up to 50% variation at some points. However individual experiments do show a universal curve is followed, F. Bodart (1975) gives data from elements between Ti to Cu using proton energies for 0.5 to 2.5 MeV which follow a single curve. With such a curve accurate values for σ_Z can be determined for all Z by extrapolation.

In using the X-ray production cross section a suitable and accurate method of normalization is required. The Faraday cup reading may be

used, however this introduces another unknown, that is the target thickness. Otherwise it is possible to monitor elastically scattered protons, for example F. Bodart (1975) uses an anulus solid state detector to measure back scattered protons. This removes the need to measure the thickness but requires knowledge of the elastic scattering cross section. At low bombarding energies, at backward angles this is dominated by Rutherford scattering which is an accurately known function of proton energy. Thus at low energies this technique is preferable over using the Faraday cup.

A third method is to use accurately made standards containing well defined quantities of single elements. With standards for all elements of interest then it is possible to overcome the requirement for a knowledge of the variation of X-ray production cross section with Z.

3.2 Target Preparation

Equation 3 applies to thin homogenous targets. The requirement for being "thin" depends on both the proton energy and the energy of the X-rays. For low energy protons (0.5 - 5 MeV) targets fitting this condition must be less than 100 $\mu g/cm^2$. Otherwise compensation for both loss of proton energy and absorption of X-rays must be made. Of the two, X-ray absorption is the larger factor particularly for self absorption of the L X-rays. The structure of the target is also an important consideration in obtaining element concentrations by recording the L series since if a particular element is in granular form rather than homogenous throughout the target differential absorption results and the calculated concentrations for those elements detected through the L series can be many factors too low. Fig. 3 demonstrates the greater importance of absorption in using the L rather than K series, the

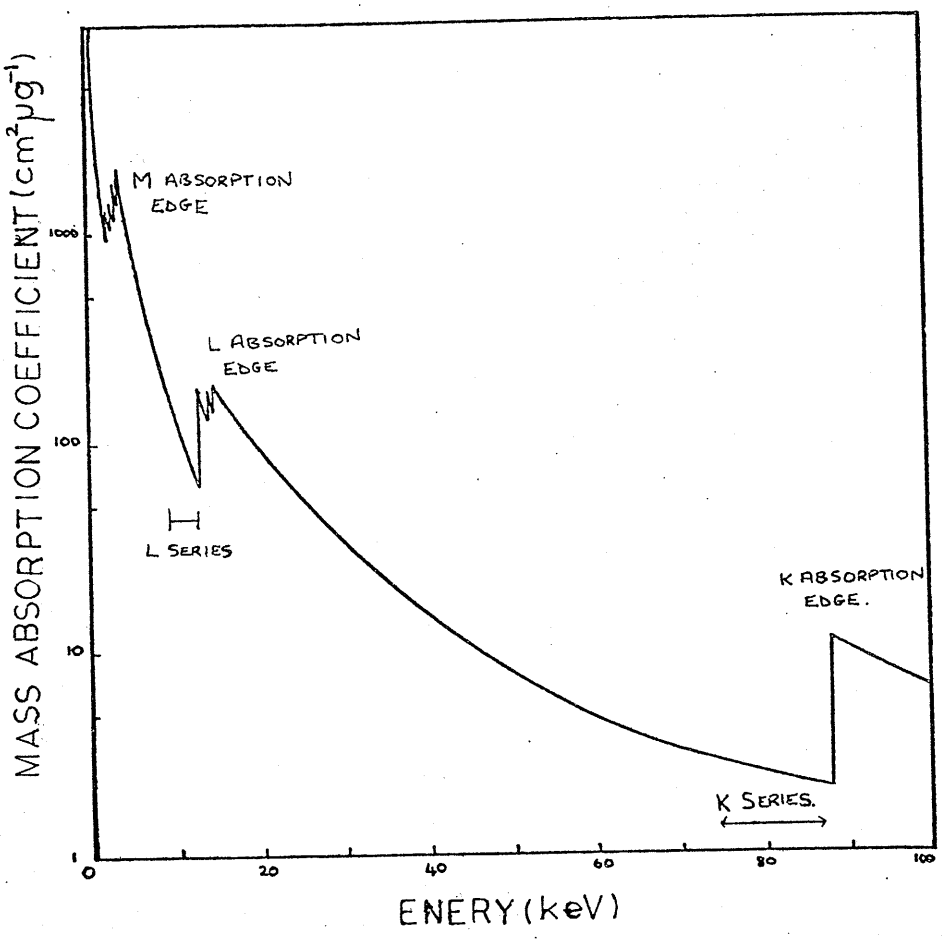

Figure 3. Mass absorption coefficient for X-rays in lead.

self absorption of the former being 2 to 3 orders greater than for the latter.

Thus the form of the target is critical towards obtaining accurate results. It is rarely possible to form self-supporting environmental targets. Normally the sample is mounted on a backing material.

The technique chosen for making targets must have the following properties:

i) Reproducibility

ii) No introduction of contaminents

iii) There should be no loss of sample in handling or under bombardment

iv) The sample should be thin* and homogenous

The backing material should have these properties:

i) low X-ray background

ii) low contamination

iii) should withstand bombardment, have good thermal and electrical conductivity.

The choice of backing material is critical in achieving the maximum sensitivity of this technique since a high proportion of the X-ray background arises from it. There are three processes which contribute.

i) proton bremsstrahlung

ii) secondary electron bremsstrahlung

iii) Compton scattering of gamma rays in the detector (see Appendix I)

At low proton energies the largest contribution to the X-ray background is from secondary electron bremsstrahlung, this results from

---

*However, thick targets are also used in which the proton beam is stopped and the relevant absorptive corrections are made.

deceleration of the free electrons knocked out in atomic ionization. The maximum X-ray energies (E_x) emitted correspond to the maximum energy transferred from the protons to the electrons on impact. That is $2m_e v^2$ therefore,

$$E_x \leqslant 2m_e v^2 \leqslant \frac{4m_e E_p}{M_p} \qquad (4)$$

which for 5 MeV protons is approximately 11 keV.

Proton bremsstrahlung extends to higher X-ray energies but is considerably lower in intensity and the Compton component is negligible because of the very low production cross section for gamma rays at proton energies below 5 MeV. A detailed study of X-ray background has been carried out by Folkmann (1974).

A variety of techniques have been applied to the problem of preparing the samples into a form which is suitable for mounting on a backing material such that it forms a thin homogenous layer. The best method depends to some extent on the type of sample. Examples are:

Wet ashing and evaporation - Johansson (1970)

Vacuum freeze drying and ashing for biological tissues and fluids - Kliwer (1972). These methods suffer from possible loss of volatile elements and the introduction of contaminants.

Slicing following use of a freezing microtone - Herman (1973). Freezing is preferable to the addition of hardening agents for slicing since the latter introduces contaminants.

To prevent loss of volatile elements the sample once attached to the backing can be covered, either by another layer of the backing material, by a lacquer, or glue or a layer of polystyrene.

One method of overcoming the requirement of a homogenous target is to produce a target holder which can be rotated, ensuring that a high proportion of the sample is analysed.

Air samples on filter paper can either be ground and formed into a target by compression, adding a small quantity of pure graphite to make the sample conducting - F. Bodart (1973). Also it is possible to put the sample directly in the beam - R.L. Walter (1974).

Backing materials commonly used are thin carbon foils (20 - 40 $\mu g/cm^2$). These are now very popular despite the fact that they are fragile, they have a low background, few contaminants and will withstand high beam currents without breakdown. Investigations have been undertaken to find suitable organic backings which would be easy to handle. Nucleopore filters have been shown to have an acceptable background and low contamination while Formvar has a very low background but higher contamination - R.L. Walter (1974).

3.3 Use of 40 MeV Protons in a Trace Element Analysis System

Advantages

i) The use of thicker targets due to higher penetration of the proton beam.

ii) The K shell ionization cross section increases sufficiently to enable the use of the K series for the detection of heavy elements.

This means:

a) It ispossible to resolve neighbouring elements with solid state X-ray detectors. This is not possible with the L series since the resolution of the detector is greater than the separation of neighbouring L lines.

b) The K series has a less complex form and for heavy elements

there is no overlap with any other series.

c) X-ray background from secondary electrons is low above the limit set by equation 4. For 40 MeV proton this limit results in a low background for the K series from elements heavier than Z = 52.

d) The absorption of the high energy X-rays making up the K series is 2 to 3 orders of magnitude lower than for the L series from the same element. This reduces the problems in accounting for absorption within the target, particularly self absorption - see Sec. 3.2.

Problems

i) 40 MeV protons will produce a high flux of gamma rays in reactions with light nuclei in the target. These will cause an X-ray background through Compton scattering in the detector (see Appendix I). If this proves to be a problem, the effect can be reduced using a Compton suppression unit with the detector.

ii) The secondary electron bremsstrahlung increases in intensity and its maximum energy changes from 11 keV to 30 keV between 3 and 40 MeV proton energy causing many problems in resolving the K series from light elements above background.

iii) Measurements of $K_{\alpha 2}:K_{\alpha 1}$, $K_{\beta}:K_{\alpha}$ and σ_z are scarce above 10 MeV proton energies and particularly above 30 MeV.

Points i) and ii) suggest a thorough investigation is necessary to establish the most suitable backing material, those used at lower energies may not necessarily be ideal.

Point iii) requires a series of measurements of these parameters as a function of Z and proton energy.

4. EXPERIMENTAL PROCEDURE

4.1 Scattering Chamber

The study of X-ray fluorescence has been carried out on line B, 30° left at the University of Manitoba cyclotron (Fig. 4). The principal focus of the quadrupoles on this line is at a β - γ spectrometer which consists of a β spectrometer and a Ge(Li) detector mounted on a turntable pivoted about a vertical axis which passes through the centre of the target. This facility appeared suitable to adaption for X-ray fluorescence work. A new face plate was designed for the β spectrometer with a curved face so that for all angles with respect to the beam the X-ray path in air is equal. The window allows detection of X-rays from 30° forward to 150° backward angle. The plate also includes a port which allows the introduction of a vertical target ladder holding 4 targets, this replaces the previous ladder which was orientated at 38° to the vertical and had only 2 target positions. A photograph of the chamber and turntable are shown in Fig. 5.

4.2 Ge(Li) Detector

An Ortec 5 mm thick planar Ge(Li) detector was purchased to study the X-ray emission. This choice was made because of its high efficiency, approximately 100% between 15 and 85 keV. Since we were primarily interested in studying X-ray fluorescence from heavier elements this is more suitable than a Si(Li) detector which has an efficiency which drops off rapidly above 20 keV. The planar arrangement being preferred from a coaxial detector since the latter is reported to have a shorter life with respect to radiation damage.

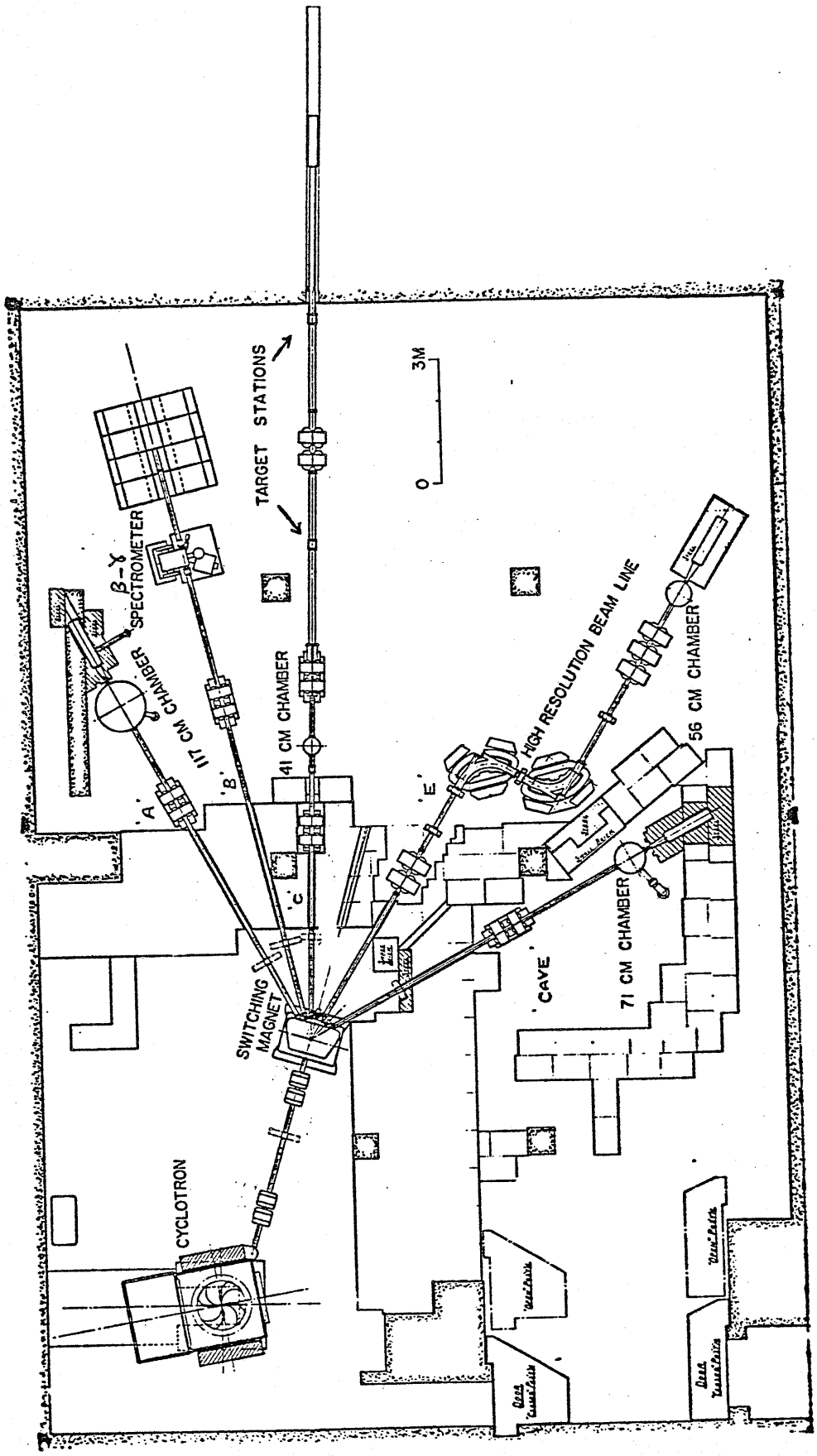

Figure 4. The experimental area at the Manitoba cyclotron.

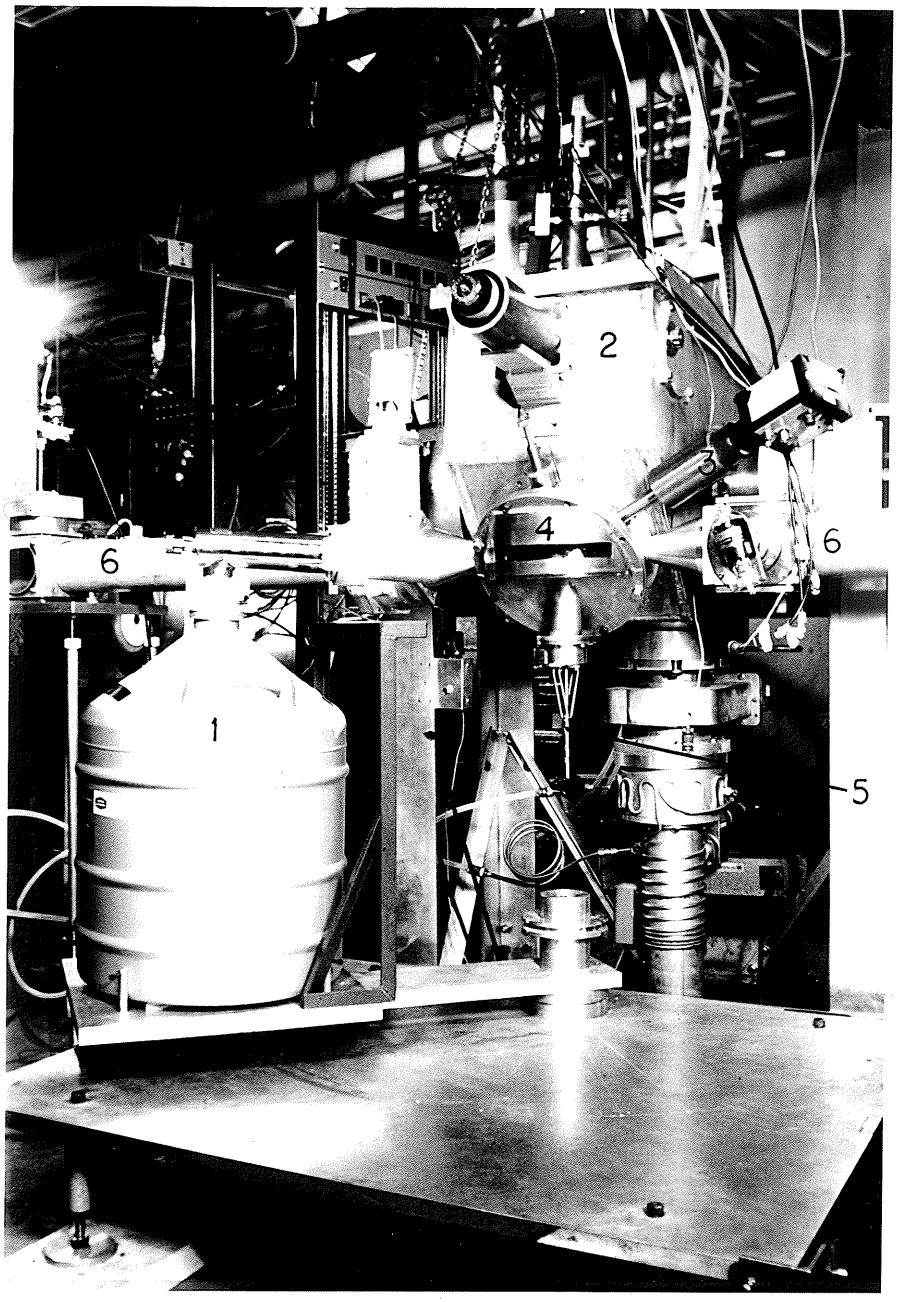

Figure 5. The β - Spectrometer. 1. Ge(Li) detector. 2. β Spectrometer. 3. Plastic Scintillator and Photomultiplier. 4. Curved Flange. 5. Target Ladder. 6. Beam line 'B'.

The specifications of the detector are:

Active surface area	: 3.14 cm^2
Active depth	: 5 mm
Operating voltage	: -1,200 volts
Full width half maximum (F.W.H.M.)	: 250 eV at 6 keV
	: 487 eV at 122 keV

We have used γ-rays and X-rays from Ba^{133} and X-rays from Cd^{109} to calibrate the X-ray detector. Using the 80 keV γ-ray from Ba^{133} we obtained a FWHM of 300 eV.

4.3 Beam Monitoring

The first series of experiments were carried out using the beam monitors set up as part of the β spectrometer (Fig. 6). The monitor consists of a plastic scintillator and photomultiplier set at 30° forward angle with respect to the incident beam. However this is only practical for a few targets since values for elastic scattering cross sections for protons with energy in the region 20 - 50 MeV are available for only a limited number of elements. Following this first experiment the integrated Faraday cup reading has been used to normalize results, this follows the connection of an electron suppression ring to the Faraday cup.

4.4 Data Taking and Analysis

The electronics is set up as shown in Fig. 6. The pulses from the Ge(Li) detector are amplified in the experimental area using an Ortec Spectroscopy amplifier, then transferred directly to the ADC's. Energy spectra being collected by the online PDP 15/20 computer using the data collection programme MIRAD. The spectrum were taken in 2048

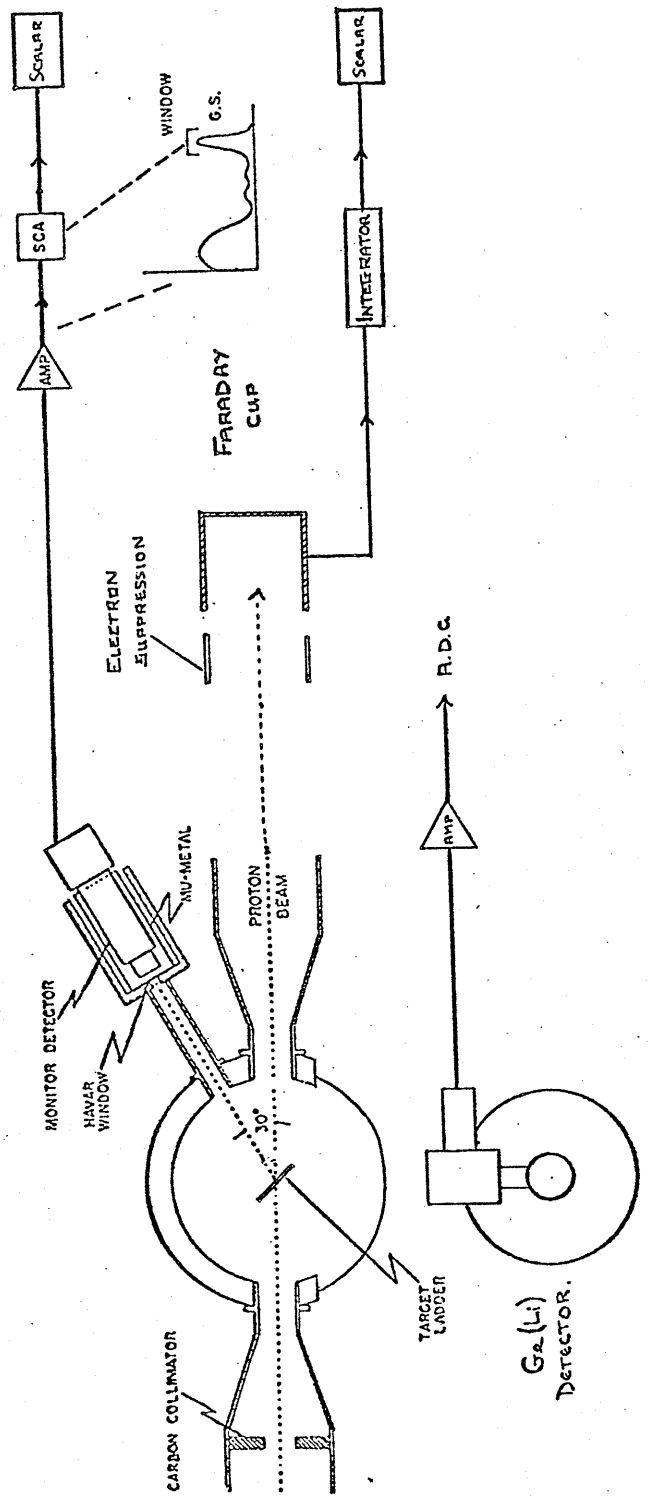

Figure 6. Schematic diagram of experimental set up.

channel binary files and stored on DEC tape and magnetic tape. The regions of interest in each spectrum were converted to ASCII files compatible with the IBM 370/44 computer at the University of Manitoba Computer Centre. These files were transferred to disc using a data transfer programme JUANDEFU and analysed using a peak fitting programme named CUTIPIE written by W. Tech (1974). This reference gives details of the various options available. The programme was written to analyse high resolution X-ray and gamma ray spectra.

A second programme written by D. Hasell* was also used, this runs on the PDP 15/40 at the cyclotron and is a simple background subtraction. Results were compared with those from CUTIPIE, agreement was very good for peaks well resolved from neighbouring peaks.

---

*Graduate student, Cyclotron Laboratory, University of Manitoba.

5. RESULTS

Our preliminary results show that we are able to obtain high resolution spectra from pure heavy element targets and that Compton background did not appear significant when using 40 MeV protons to induce the fluorescence. Typical spectra are shown in Fig. 7.

A series of measurements have been taken on pure targets to obtain values for $K_\beta:K_\alpha$, $K_{\alpha_2}:K_{\alpha_1}$ and σ_z for proton bombarding energies between 20 and 50 MeV, these have been compared with extrapolations from low energy data. Four targets were studied, self separating foils of 5 mg cm^{-2} lead and 4 mg cm^{-2} tantalum plus samples of 0.6 mg cm^{-2} gold and 0.56 mg cm^{-2} indium mounted on a 0.5 mil Mylar backing. Typical beam currents on target were between 0.2 and 1 nA in order to keep count rates low.

5.1 $K_\beta:K_\alpha$, $K_{\alpha_2}:K_{\alpha_1}$ ratios

Our values for these ratios are given in Table 1 and 2. A comparison is made with values obtained from other ionization processes, both X-ray and radioactive source induced fluorescence, with the values of Rao (1972) obtained through a least squares fit to the data from 12 experiments and with the theoretical calculations of Scofield (1969). Our results show good agreement with these, lying within the limits covered by these other results to within our experimental error. The accuracy is not sufficient to detect any dependence of these ratios on the proton bombarding energy. This last point enables the use of the values obtained at low proton energies in interpreting fluorescence spectrum from environmental samples when using 40 MeV protons.

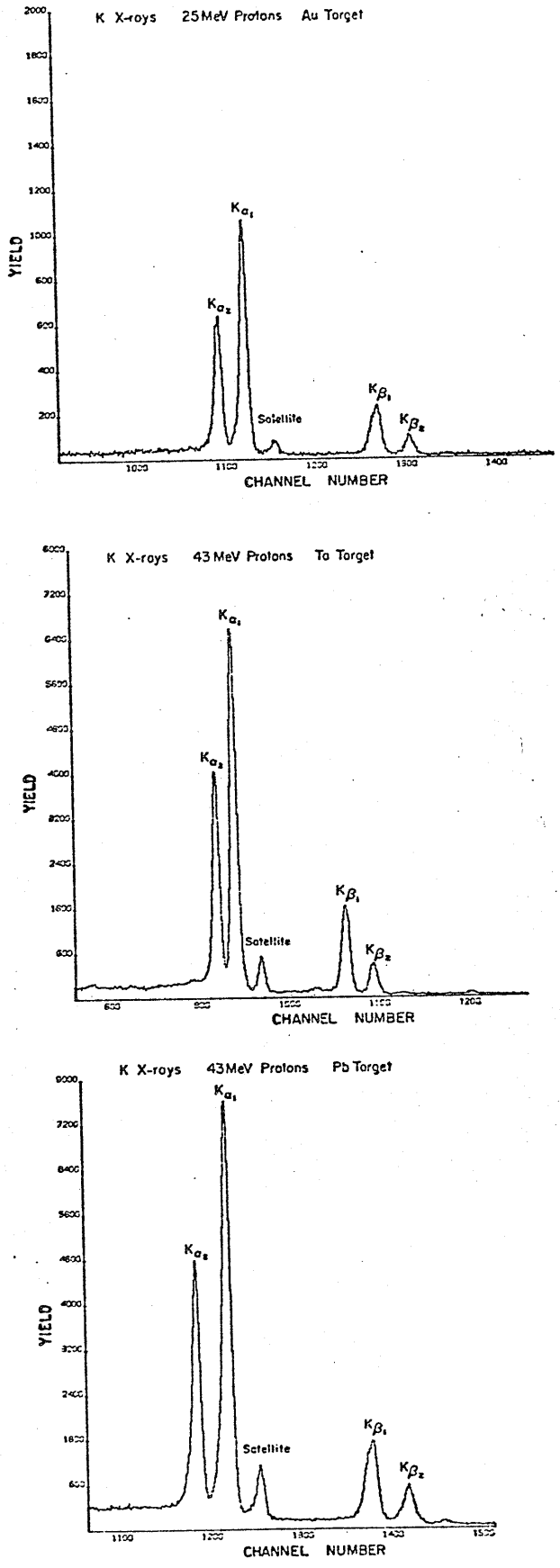

Figure 7. Typical spectra from Pb, Au, and Ta

TABLE 1.

K_β : K_α Ratios

Target	Present Work	Other results: excitation by- X-rays*	Radioactive source**	Rao (1972)	Theory Scofield (1969)
Pb	0.280 ± 0.006	0.271	0.2810 ± 0.0056	0.279	
Au	0.254 ± 0.014	0.279	0.2734	0.276	0.264
Ta	0.257 ± 0.02		0.2615 ± 0.0052	0.269	
In	0.227 ± 0.009		0.2192	0.217	0.200

* Slivinsky (1969) ** Hansen (1970)

TABLE 2.

K_{α_2} : K_{α_1} Ratios

Target	Present Work	Other results: excitation by- X-rays*	Radioactive source**	Rao (1972)	Theory Scofield (1969)
Pb	0.606 ± 0.02	0.61 ± 0.01	0.596	0.592	0.5960
Au	0.60 ± 0.04	0.6 ± 0.01	0.585	0.586	0.588
Ta	0.53 ± 0.09	0.58 ± 0.02	0.554	0.573	0.574

* Ebert (1969) ** Nelson (1969)

5.2 Ionization Cross Sections

Values for this have been obtained for lead and gold as a function of energy between 20 and 50 MeV. These values are plotted in Fig. 8 on the universal plot discussed in Sec. 2.1. The results are compared directly with the experimental results of F. Bodart (1975) and G.A. Bissinger (1972). Our results follow their results well within the combined experimental errors. A more extensive study is planned which will extend the points to a value for η of 5.4 using targets ranging from Ti to Pb. This complete curve will then be compared with the predictions of the B.E.A. and B.A. theories. However the excellent agreement shows that a universal curve can be drawn up for all elements and thus the cross sections for X-ray production for any target can be extrapolated from this plot.

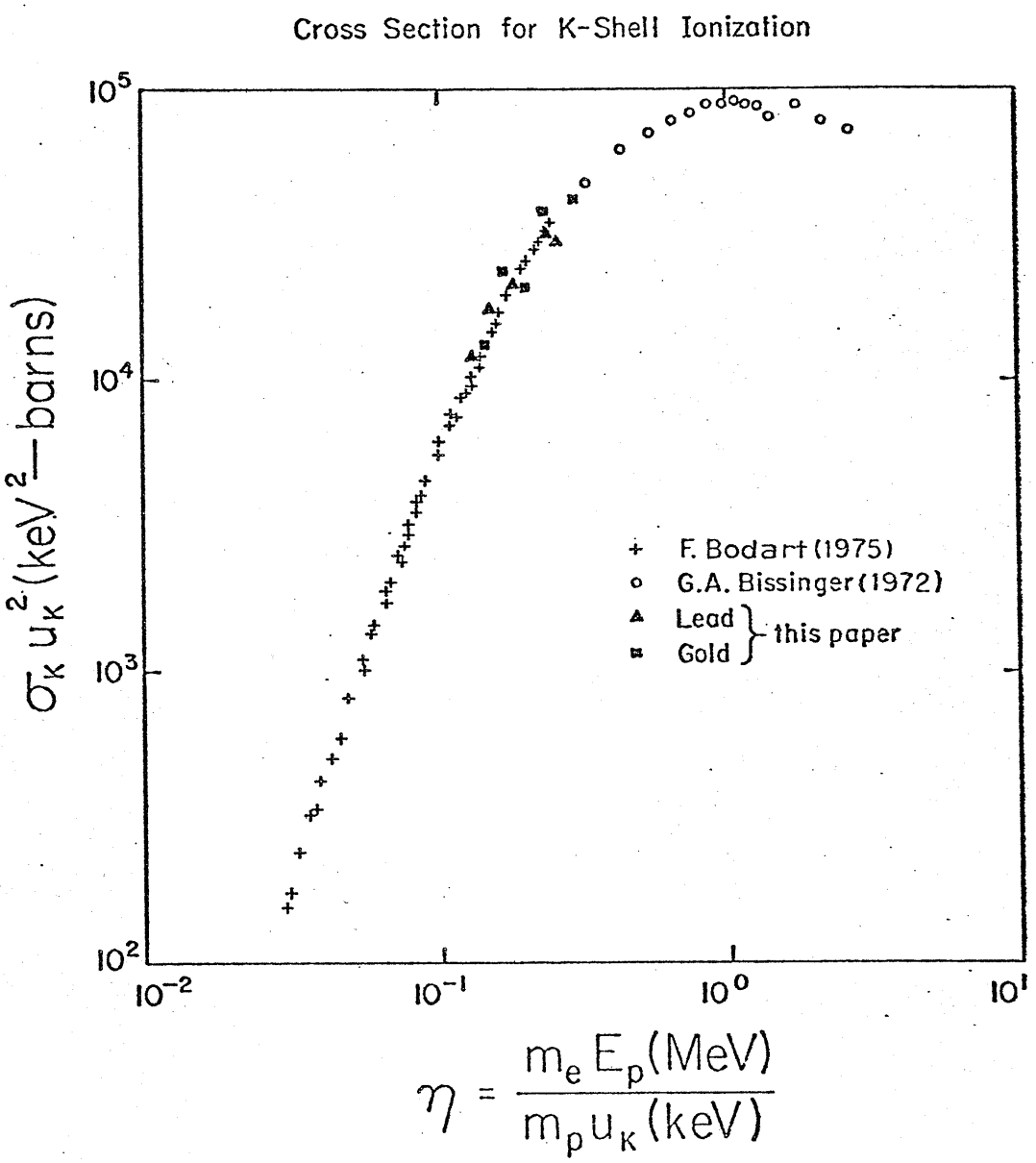

Figure 8. Relative ionization cross sections for lead and gold.

6. THE IDENTIFICATION OF THE NATURE OF A SATELLITE PEAK

Fig. 7 shows a satellite peak cleanly resolved on the high energy side of both the K_{α} and K_{β} X-ray groups. These peaks cannot be explained through the normal allowed transitions. We have undertaken a study of this effect using a tantalum target and proton energies between 20 and 45 MeV in order to determine its production mechanism.

Our results are described in detail in a paper published in the Journal of Physics G vol. 2 (1976). A reprint of this paper follows.

MS 51(G247L)
J. Phys. G: Nucl. Phys., Vol. 2, No. 1, 1976. Printed in Great Britain. © 1976

LETTER TO THE EDITOR

The nature of a K x-ray satellite peak is determined from the analysis of fluorescence spectra induced by 20–50 MeV protons

C P Randell, J S C McKee and S F J Wilk
Cyclotron Laboratory, Department of Physics, University of Manitoba, Winnipeg, Manitoba RwT 2N2, Canada

Received 1 March 1976

Abstract. A satellite peak resolved on the high-energy side of K_α and K_β x-ray groups excited by 20–50 MeV protons in tantalum is studied, and its production mechanism is determined to be the result of de-excitation by internal conversion of the product nuclei from (p, xn) reactions.

Satellite peaks associated with the production of K_α and K_β x-rays in proton-induced fluorescence spectra have currently become the subject of considerable interest and research effort. Such peaks have been observed in a recent experiment at this laboratory designed to measure the total K x-ray production cross sections for heavy elements bombarded with 20–50 MeV protons. We have now attempted to determine the production mechanism for a particular satellite through measurement of the energy separation from normal K_α peaks, ΔE_s, and the energy dependence of the cross section.

A recent paper (Dyson 1975) comments that a satellite can be caused by the de-excitation of an atom with a doubly ionized K shell. The first electron making a transition from the L shell can experience a larger potential difference than normal, namely $E_{K_\alpha} + \Delta E_s$, due to the reduced screening caused by the absence of both K-shell electrons. This effect has recently been reported (Richard *et al* 1972).

Wölfli *et al* (1975) have demonstrated the presence of a further phenomenon, namely double ionization resulting in the simultaneous transition of two electrons from the L to the K shell producing a single photon of energy $2E_K + \Delta E_s$, or alternatively $E_{K_\alpha} + E_{K_\beta} + \Delta E_s$. Again the factor ΔE_s is caused by the reduced screening seen by the L-shell electrons in the absence of two rather than one K-shell electron. Neglecting fine structure splitting, ΔE_s for the K_α transition is given by

$$\Delta E_s = 13{\cdot}6\,[Z^2 - (Z - s)^2] \times \tfrac{3}{4}\,\text{eV} \qquad (1)$$

where s is the screening factor, and takes the value $\frac{5}{16}$ for K-shell screening.

A second production mechanism for the satellite peak has been suggested (Deconninck and Longequeue 1973). The daughter products from (p, xn) reactions have excitation energies of the order of 5 MeV, and the de-excitation which follows occurs through either gamma ray emission or internal conversion. The latter process can result in K-shell ionization followed by K x-ray emission with energy equivalent

to that from an atom with the charge of the reaction product, giving

$$\Delta E_s = E_K(Z + 1) - E_K(Z). \tag{2}$$

We have studied x-ray fluorescence spectra induced in tantalum by 20–50 MeV protons, since complete measurements of ^{181}Ta (p, xn) cross sections already exist. The experimental arrangement was similar to that commonly used in proton-induced x-ray work. A 5 mm planar Ge(Li) detector was positioned at 90° to the proton beam. It had an area of 3·14 cm^2 and a resolution of 487 eV for 122 keV gamma rays. The proton beam was monitored by a plastic scintillator set at an angle of 30° forward with respect to the beam. A self-supporting target of 4 mg cm^{-2} tantalum was used.

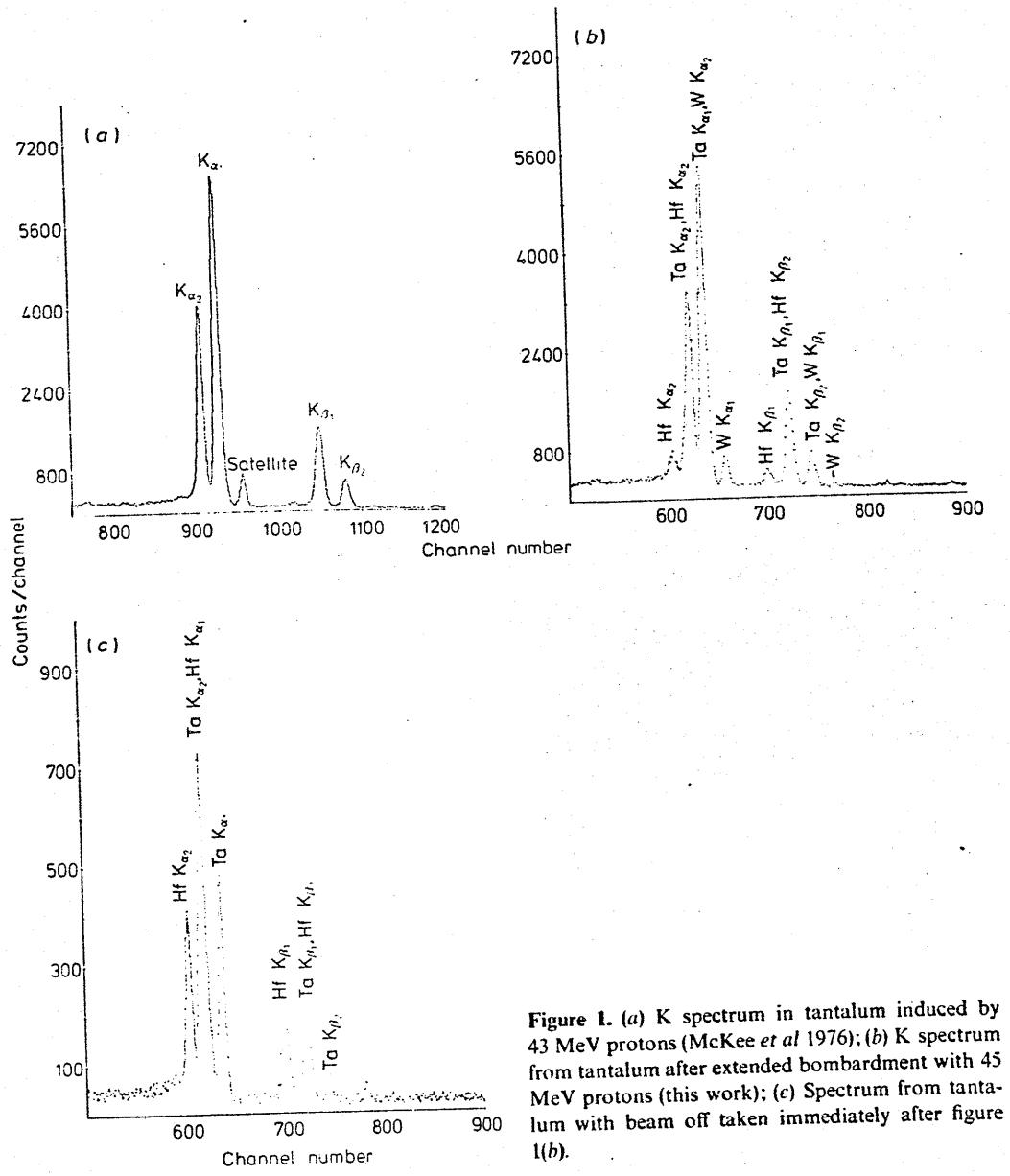

Figure 1. (*a*) K spectrum in tantalum induced by 43 MeV protons (McKee *et al* 1976); (*b*) K spectrum from tantalum after extended bombardment with 45 MeV protons (this work); (*c*) Spectrum from tantalum with beam off taken immediately after figure 1(*b*).

In the experiment a single satellite was resolved on the high-energy side of the K peaks as shown in figure 1(*a*). Analysis of these data yields a value for ΔE_s of 1·8 keV, indicating that the satellite is the K_{α_1} x-ray emission line from tungsten; the K_{α_2} peak is obscured by the overlying tantalum K_{α_1} peak. A second satellite is barely discernable on the high-energy side of the K_{β_2} peak which corresponds to the tungsten K_{β_2} line. The energy difference expected from double ionization as given by equation 1 would be 0·468 keV.

Further evidence concerning the origin of these satellites is found in the experimental observation that de-excitation of the product nuclei from the (p, *x*n) reaction is observed following an extended period of bombardment. At this time satellites appear on the low-energy side of both K_α and K_β groups corresponding to the K_{α_2} and K_{β_1} x-rays from Hf as shown in figure 1(*b*). By recording spectra with beam off, see figure 1(*c*), it becomes apparent that the low-energy satellite results from de-excitation of a daughter nucleus following the decay of nuclei produced in the initial reaction. One such decay scheme which is clearly identified through associated low-energy gamma rays is the following

$$^{181}\mathrm{Ta(p,\gamma n)}^{178}\mathrm{W} \rightarrow {}^{178}\mathrm{Ta} \rightarrow {}^{178}\mathrm{Hf}.$$

Finally, the energy dependence of the total cross section for production of all satellites resulting from (p, *x*n) reactions has been measured. The K_{α_2} and K_{β_1} satellites, which are obscured by the tantalum K_{α_1} and K_{β_2} peaks respectively, are taken into account assuming K_{α_2}:K_{α_1} and K_{β_2}:K_{β_1} ratios of 0·575 (Rao *et al* 1972) and 0·249 (Middleman *et al* 1970). Figure 2 shows a comparison between these data

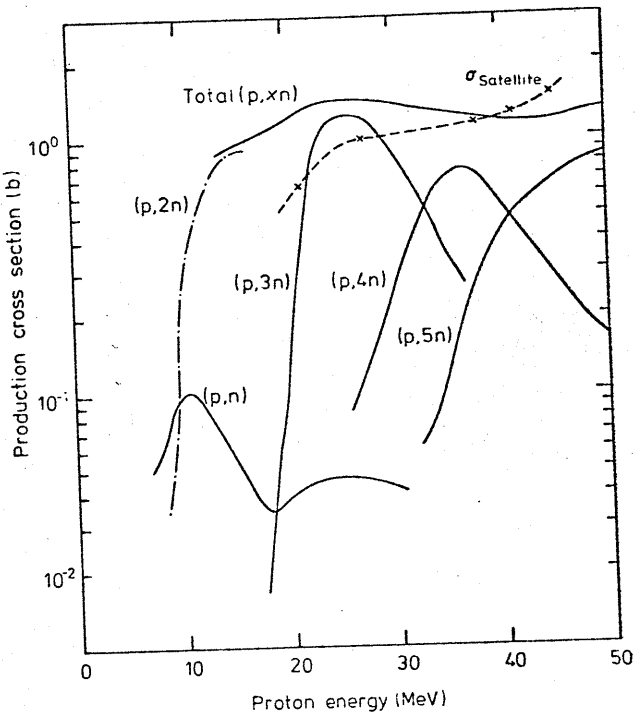

Figure 2. Total cross section for all K satellite peaks resulting from (p, *x*n) reactions (broken curve) is compared with (p, *x*n) total cross sections measured by Rao and Yaffi (1963) (full curve) and (p, 2n) measured by Chodil *et al* (1967) (chain curve).

and various (p, xn) reactions. Owing to the complexity of the individual energy level schemes for the different reaction products, it is difficult to estimate the internal conversion coefficient for the decay of each to the appropriate ground state. Thus it cannot be stated categorically that the observed energy dependence is that to be expected for the system under study. Nonetheless, the experimental observations made are sufficient to demonstrate that the satellite arises from (p, xn) reactions and that the energy dependence shown in figure 2 can enable an estimation of the overall internal conversion coefficient for each product nucleus to be made.

The double ionization cross section is clearly too small for its effect to be observed.

References

McKee J S C, Randell C P and Wilk S F J 1976 *Analytical Chemistry* to be published
Dyson N A 1975 *Phys. Med. Biol.* **20** 1
Richard P, Hodge W and Moore C F 1972 *Phys. Rev. Lett.* **29** 393
Wölfli W, Stoller Ch, Bonani G, Sutter M and Stöcjli M 1975 *Phys. Rev. Lett.* **35** 656
Deconninck G and Longequeue N 1973 *Phys. Rev. Lett.* **30** 863
Rao P V, Chen M H and Crasemann B 1972 *Phys. Rev.* A **5** 997
Middleman L M, Ford R L and Hofstadter R 1970 *Phys. Rev.* A **2** 1429
Rao C L and Yaffe L 1963 *Can. J. Phys.* **41** 2516
Chodil G, Jopson R C, Mark H, Swift C D, Thomas R G and Yates M K 1967 *Nucl. Phys.* A **93** 648

7. PRELIMINARY INVESTIGATION FOR THE ESTABLISHMENT OF A TRACE ELEMENT ANALYSIS SYSTEM

Having shown that we are capable of obtaining a high resolution spectrum following bombardment of pure elements with 20 - 50 MeV protons, and with the measurements obtained for $K_\beta : K_\alpha$, $K_{\alpha 2} : K_{\alpha 1}$ and σ_z we are now in a position to investigate the final requirement for a high sensitivity accurate trace element analysis system. That is to find a suitable method for preparation of environmental samples and a backing material which produces a minimum background and has insignificant contaminents above Z = 15.

Two methods have been studied to date. The first was to form a mixture of 98% borax, 2% graphite. This is ground with a mortar and pestle, then 100 mg was weighed, and compressed into a 1.9 cm diameter pellet in a die by a pressure of approximately 20,000 p.s.i. forming a target 9 mg cm^{-2} thick. Borax is a salt ($Na_2B_4O_7.10H_2O$) extracted from lake deposits, particularly in California; after heating it forms a glass like material. It was used for this latter property since under high pressure it forms a strong glassy disk. The graphite was normal commercially available graphite sold as a dry lubricant. This was added to ensure that the target is conducting, avoiding charging which can cause increased bremsstrahlung. It was intended that this would be a suitable method for target preparation in the analysis of air samples collected on filter paper. These would either be ground or ashed, added to the mixture before being ground and compressed, thus ensuring a homogenous target is formed.

A typical spectrum is shown in Fig. 9. This was obtained through bombardment of one of these pellets by a 1 nA beam of 43 MeV protons.

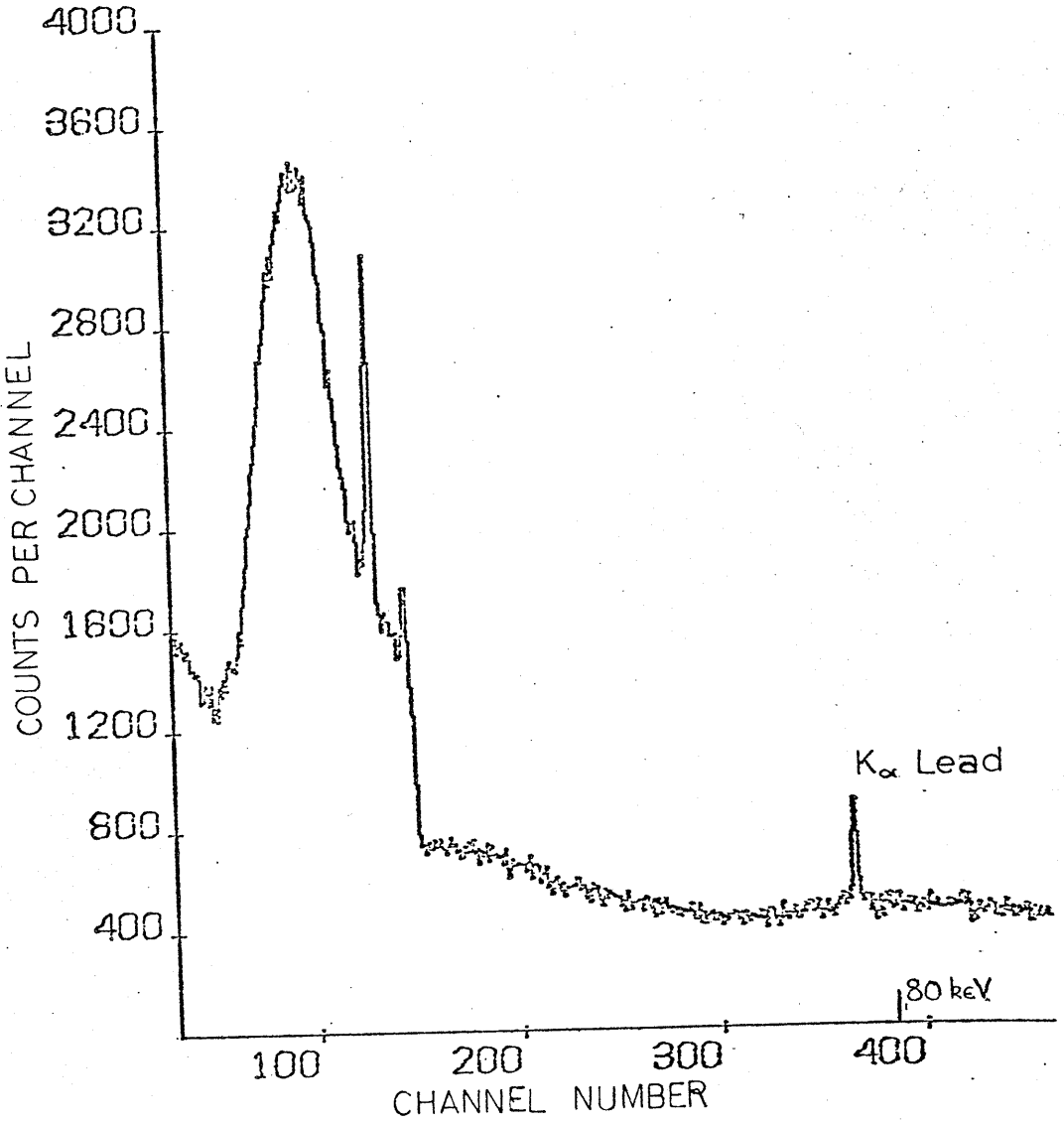

Figure 9. Background spectrum from borax-graphite pellet following bombardment by 45 MeV protons.

The single peak at channel 380 shows that the pellet has a very high impurity level of lead, we have estimated this to be approximately 200 ppm. It has since been shown that this is predominantly due to the graphite, suggesting a 2% contamination of the normal commercially available graphite.

The second method studied for analysing air samples was to place Millipore filters directly in the beam. The filter was first sprayed with a lacquer which would prevent the loss of the sample from the filter surface. Soluvar was used, this contains Aluminium which helps with the prevention of charging of the sample. A typical spectrum is shown in Fig. 10. This shows no perceptible heavy element contamination, the background is significant, and it should be possible to improve on this using thinner backing materials. A second problem of using millipore filters for air samples is that, with the pumps commonly used to collect these samples, the sample is not homogenously distributed across the paper, there being a higher concentration at the centre.

The results from these two methods demonstrate two points.

i) The background above 30 keV is very low in comparison to below, demonstrating that the K series will be observable for heavy elements for concentrations of approximately 1 ppm. To enable the measurement of concentrations for elements lighter than Z = 52 for which the K series lies in this region of high intensity background further investigation is required using suitable absorbers and very low count rates. This will mean using beam currents of approximately 0.2 nA

ii) The background in the region above 30 keV although considerably lower than below 30 keV is higher than anticipated due to proton bremsstrahlung. This suggests that a second component is present, that is a component due to Compton scattering. The size of this component

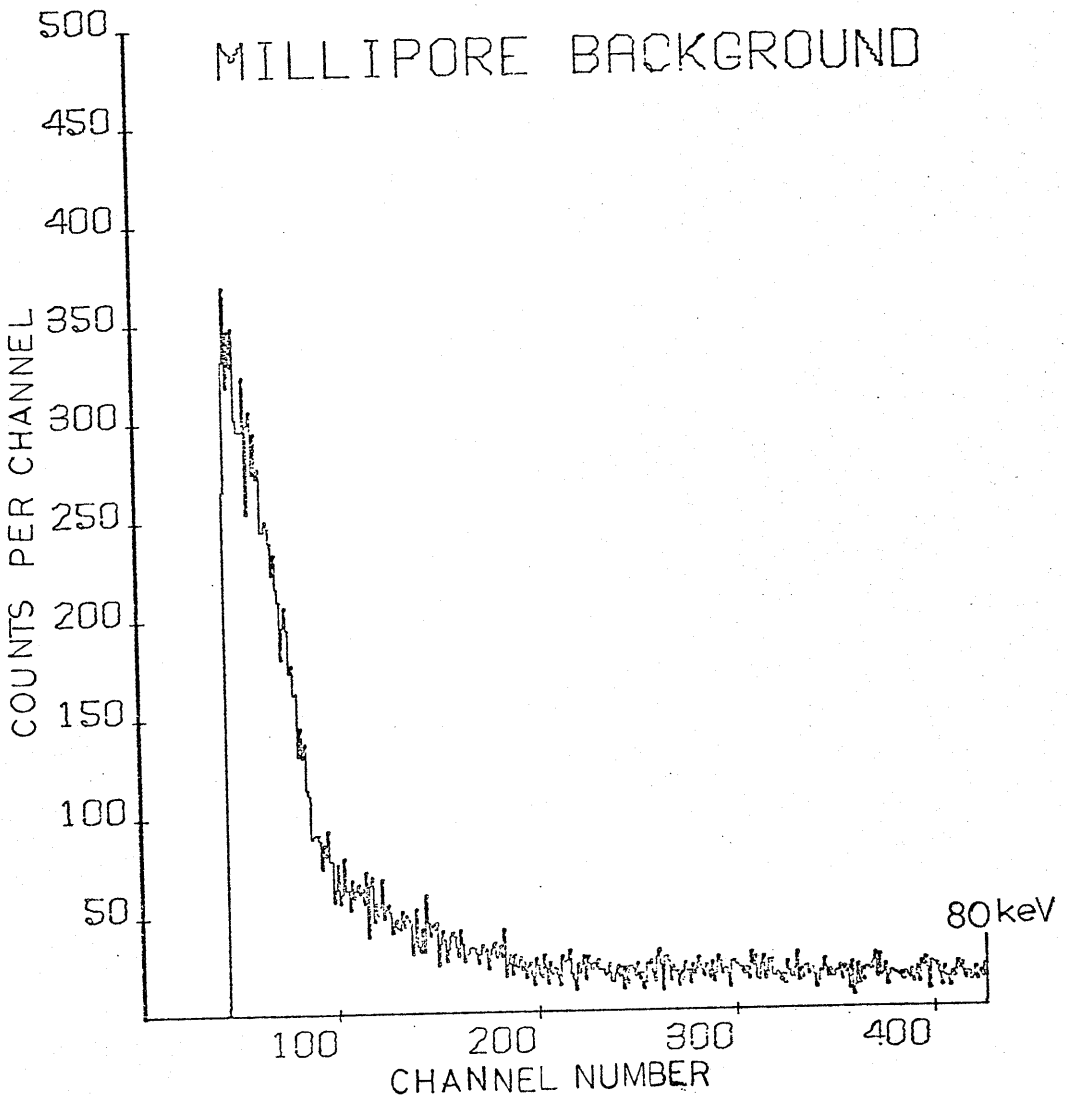

Figure 10. Background spectrum from millipore filter following bombardment by 43 MeV protons.

is dependent on the backing materials, with further investigation it is hoped that this can be reduced.

CONCLUSION

Our measurements of $K_\beta : K_\alpha$, $K_{\alpha 2} : K_{\alpha 1}$ ratios and the K shell ionization cross section shows excellent agreement with extrapolation from lower proton energy data. This means that in analysing unknown samples through the collection of X-ray fluorescence spectrum induced by 40 MeV protons the values for these parameters for all Z can be obtained through extrapolation from the abundance of results existing between 0,5 and 5 MeV proton energies rather than it being necessary to make a complete series of measurements for a wide range of Z. However as mentioned in Sec. 5.2 it is planned to make a thorough study of the ionization cross section particularly for low as well as high Z so that a complete comparison with theory can be made.

Our initial studies for preparation and backing of environmental samples has been limited but has been sufficient to point out the two problems outlined in detail in Sec. 7. The results suggest it should be possible to obtain values for concentrations of heavy elements down to 1 - 10 ppm, however it is anticipated that more suitable backing materials could lower this by a factor of 10. Also it is apparent that the large increase in background from secondary electron bremsstrahlung below 30 keV causes problems in the analysis for light elements at the 1 - 10 ppm range which is easily obtainable by lower proton energies.

Also it should be noted that the satellite peak which is resolved for elements of $Z > 60$ will not cause significant problems and does not effect the advantages outlined in Sec. 3.3. The satellite is 2 to 3 orders of magnitude smaller than the parent element, thus with a limit to sensitivity of 1 ppm a concentration greater than 100 ppm would be

required before this peak could be resolved, and in knowing the relative cross sections it is a simple matter to compensate for this peak in the presence of high concentrations of neighbouring elements.

CHAPTER II

THE DESIGN OF A MAGNETIC REGENERATOR WHICH WILL ENABLE THE ACCELERATION OF POSITIVE IONS FROM THE MANITOBA CYCLOTRON

1. POSITIVE ION ACCELERATION

The normal method for extraction of a positive beam which has been accelerated to the required energy in the cyclotron magnetic field is to position an electrostatic deflector in such a way as to remove the proton beam from the magnetic field and direct it to an external beam line. However the turn-to-turn separation in the Manitoba cyclotron is 0.2 mm, making it impossible to use a deflector since a very high proportion of the beam would be lost into the deflector itself.

One method of increasing the turn-to-turn separation which has been successfully developed is the introduction of a perturbing field at two points in the proton orbit, one outwards and one inwards (see Fig. 11). The outward force is produced by an electrostatic plate which is known as the "peeler". The inward force cannot be applied by such an arrangement since the positive potential required results in a build up of electrons causing breakdown. Instead a magnetic perturbation is introduced by means of shaped ferromagnetic pieces placed symmetrically above and below the median plane of the cyclotron. The magnetic moment induced in these causes a local increase in the magnetic field producing an inward deflection in the proton orbit. This arrangement is known as "the magnetic regenerator". In the Manitoba cyclotron these two perturbing forces would be applied at two points subtending an angle of 90° at the centre of the cyclotron, both in the hill region of the magnetic field. The turn-to-turn separation would then be increased sufficiently to allow the positioning of an electrostatic deflector in the valley region.

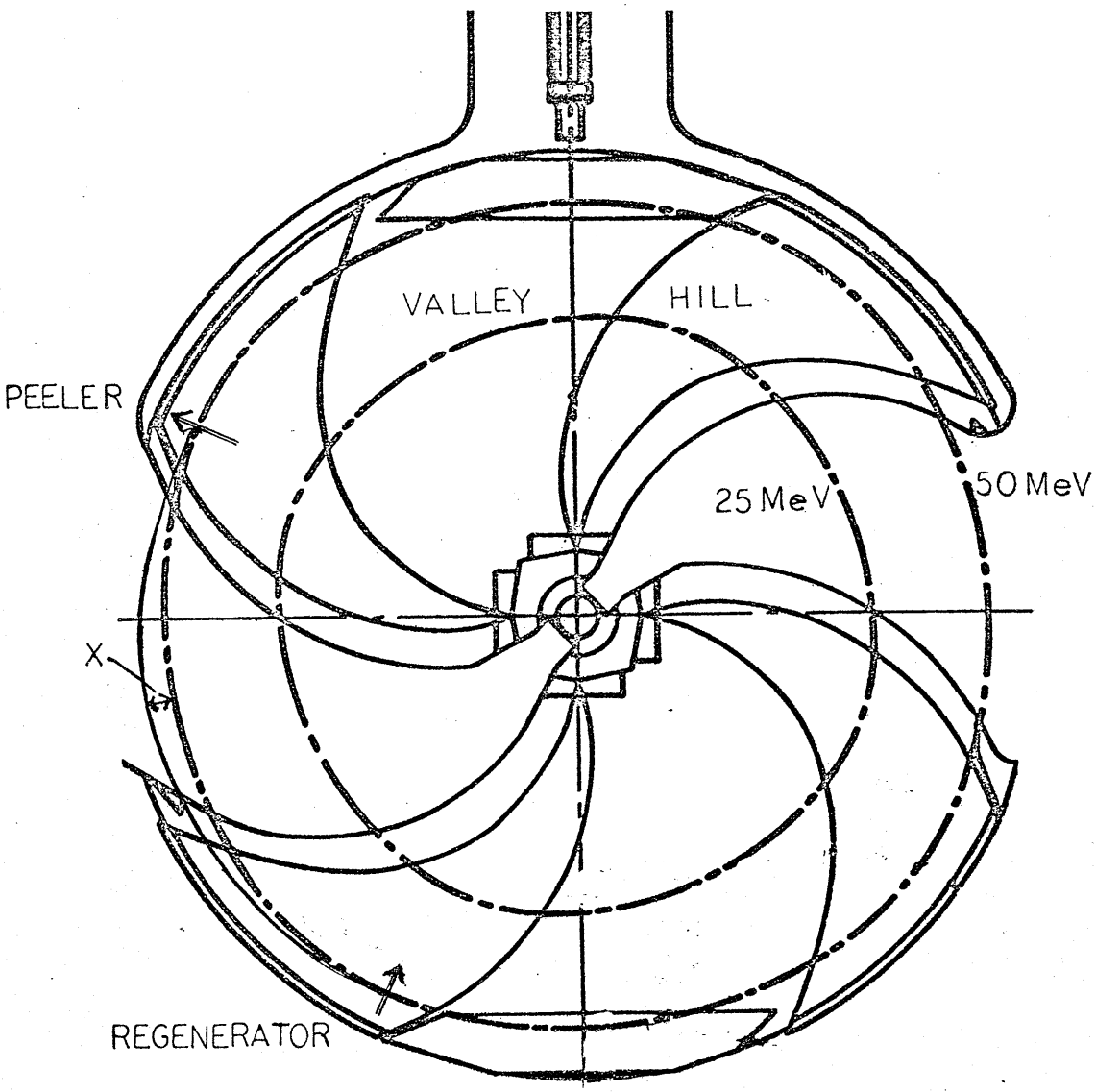

Figure 11. Peeler-regenerator location in cyclotron.

The acceleration of positive rather than negative ions in the Manitoba cyclotron would result in an increased beam intensity since the flux of positive ions from a duoplasmatron is more than one order of magnitude greater than that of negative ions. However, the use of the regenerator-peeler method is inflexible since it is necessary to design the system for a specific energy.

A computer program has been written to design a suitable magnetic regenerator. The desired shape for the perturbing field has been obtained and a simplified proton orbit program written to determine the resulting turn-to-turn separation.

2. OUTLINE OF THE PROGRAM

2.1 Field Mapping and Proton Deflection

As mentioned above the first task was to design a regenerator which produces the required field shape. The important quantity in determining the size and shape of the regenerator is to what extent a beam of protons is deflected from a circular orbit by the perturbing field, this deflection is proportional to the integral of the perturbing field along the path which the protons follow.

The program is outlined in Table 3 and is reproduced in Appendix II. Fig. 12 shows the set up of the regenerator. The initial program included only the largest pair of spheres, the effect of the secondary pairs being added afterwards. The number, size and position of the spheres being chosen to achieve the required field shape.

The program calculates the deflection of a proton moving in a straight line through the regenerator field. The deflection is calculated for 50 parallel paths separated by 1 mm. The first path is that which passes through the central axis (path 1 in Fig. 12a). The final path is that which has a closest approach, Y, of 5 cm (path 50 in Fig. 12a). The deflection in the path as the proton passes through the regenerator is neglected in calculating the position with respect to the regenerator. The coordinates of the path are calculated at 1 mm intervals, the array Z1(K) recording the distance of each point from the central axis of the regenerator, the values of this array are limited to 5 cms, the parameters M and N recording the limits on the path such that

$Z1(M) \leqslant 5$ cm $\qquad Z1(M+1) > 5$ cm

$Z1(N) \leqslant 5$ cm $\qquad Z1(N-1) > 5$ cm.

Table 3.

FIELD MAPPING and PROTON DEFLECTION

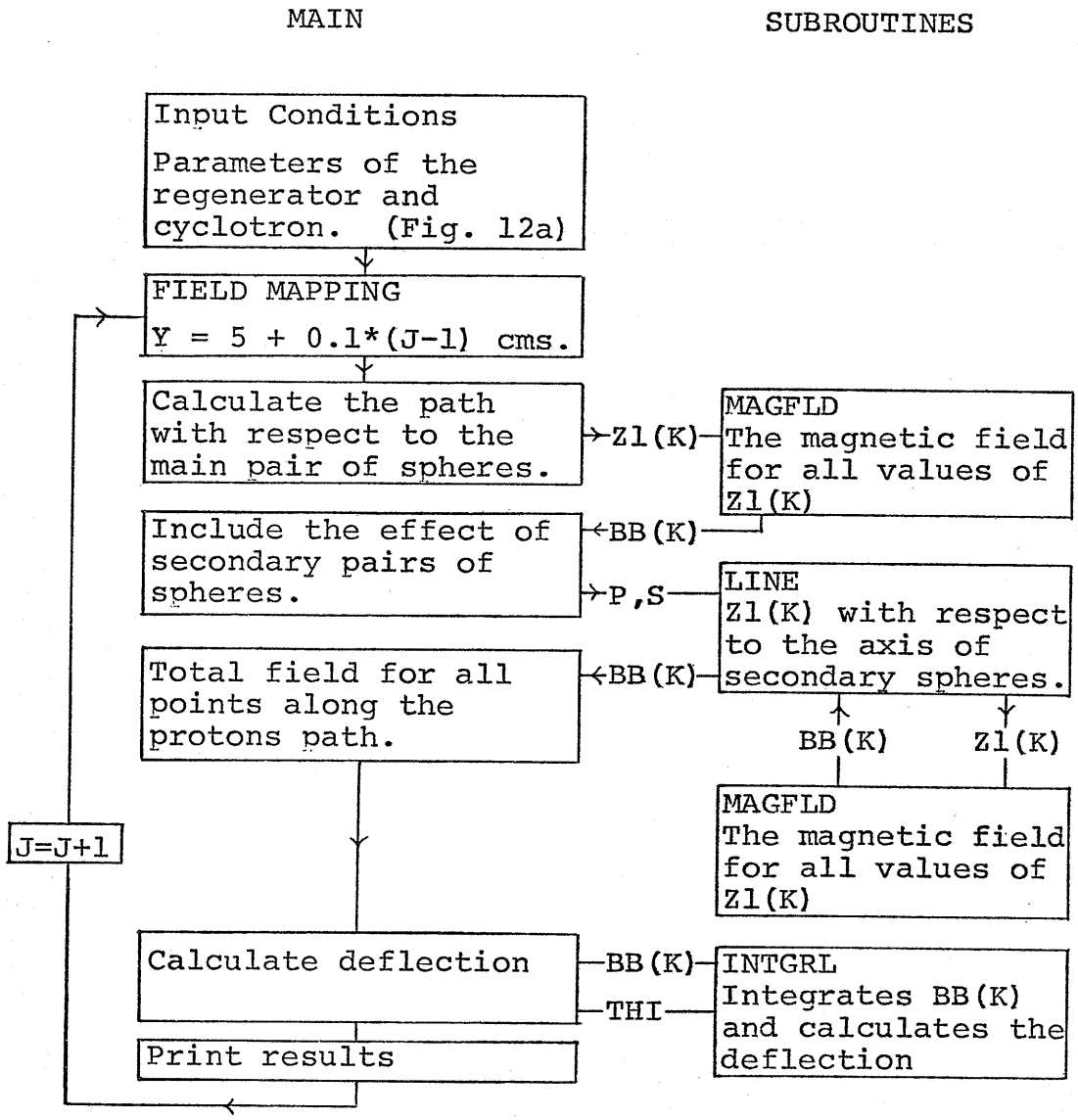

Figure 12a.

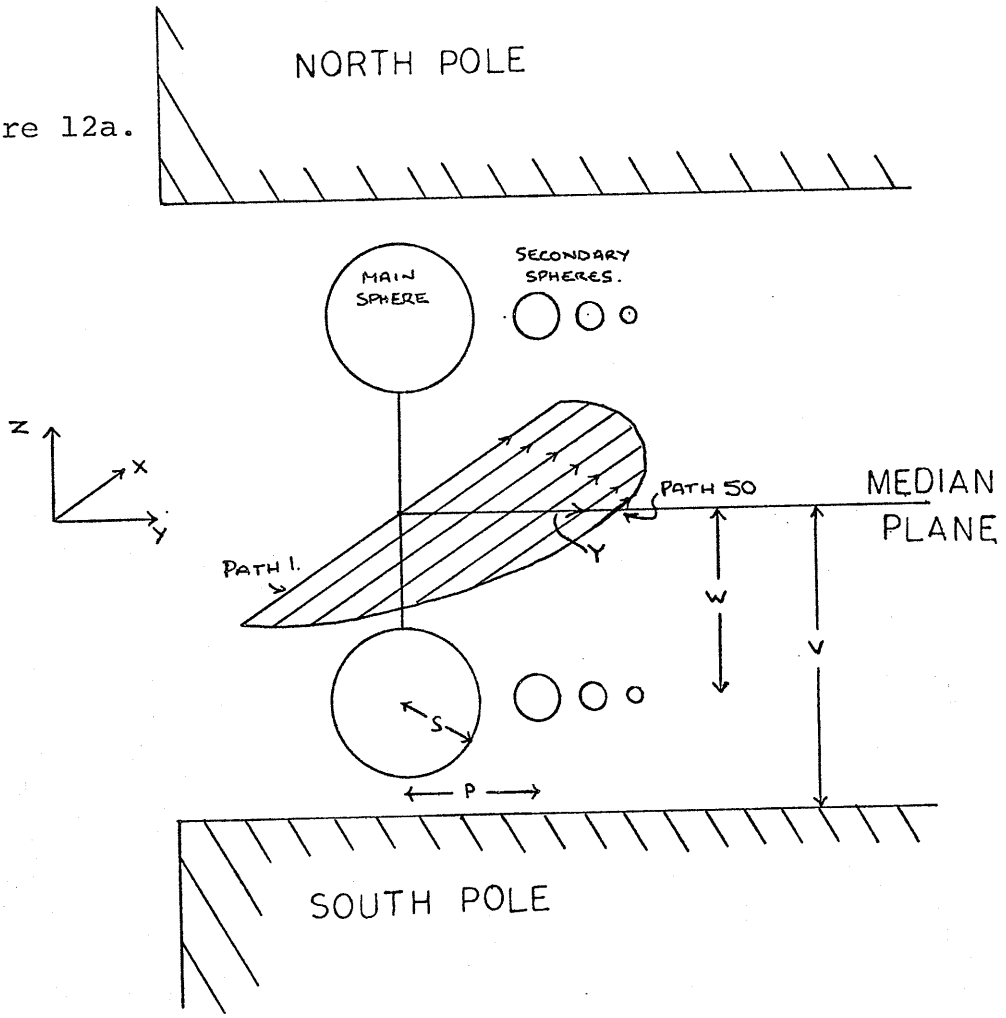

Figure 12b.

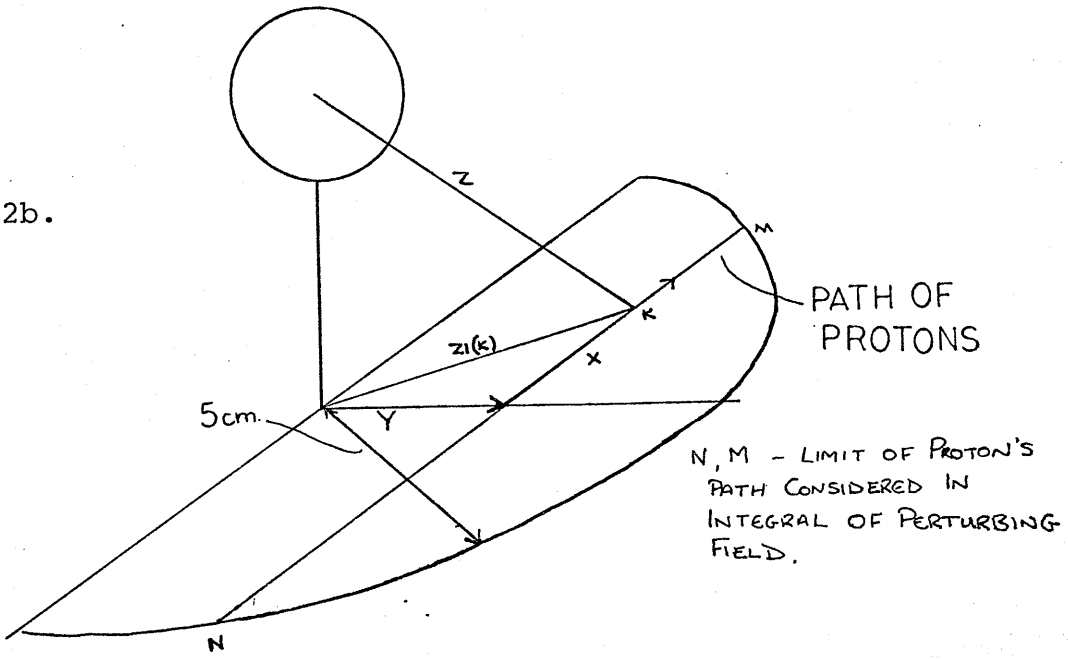

Regenerator parameters used in program.

The field caused by the main spheres of the regenerator is then calculated at each point using the subprogram MAGFLD.

The magnetic field of the regenerator is calculated using the image method in analogy with electrostatic images. The field at the median plane between the two spheres is parallel to the central axis of the spheres, the z axis in Fig. 12. Thus the field at the median plane is double the z component of a single sphere, all components in the x-y plane cancelling for the double sphere arrangement. MAGFLD calculates this component assuming the magnetic moment induced in the sphere by the cyclotron field causes the sphere to act as a simple dipole. In the DO-Loop denoted by L the value of L = 1 calculates the z component of the field caused by a free magnetic dipole and L = 2, 3, 4 .... adds the effect of successive reflections of the dipole at the two pole faces. At each reflection the dipole moment is reduced by a factor F given by:

$$F = \frac{\mu - 1}{\mu + 1}$$

where μ is the permeability of the material of the cyclotron poles.

The total perturbing field at the median plane is then recorded for each value of Z1 (K) in the array BB (K) by doubling the z component of the single sphere and its reflections.

This field is then integrated along the path of the proton in the subprogram INTGRL and the deflection this would cause is calculated assuming the velocity of the proton is that which a proton would have in a magnetic field BA at a radius R1. The deflection calculated in this way for a single sphere is shown in Fig. 13. In passing through the regenerator a deflection of 2.8° is achieved, however for values of Y greater than 13 mm an outward deflection results due to the negative perturbation in the cyclotron field caused by the dipole field for large

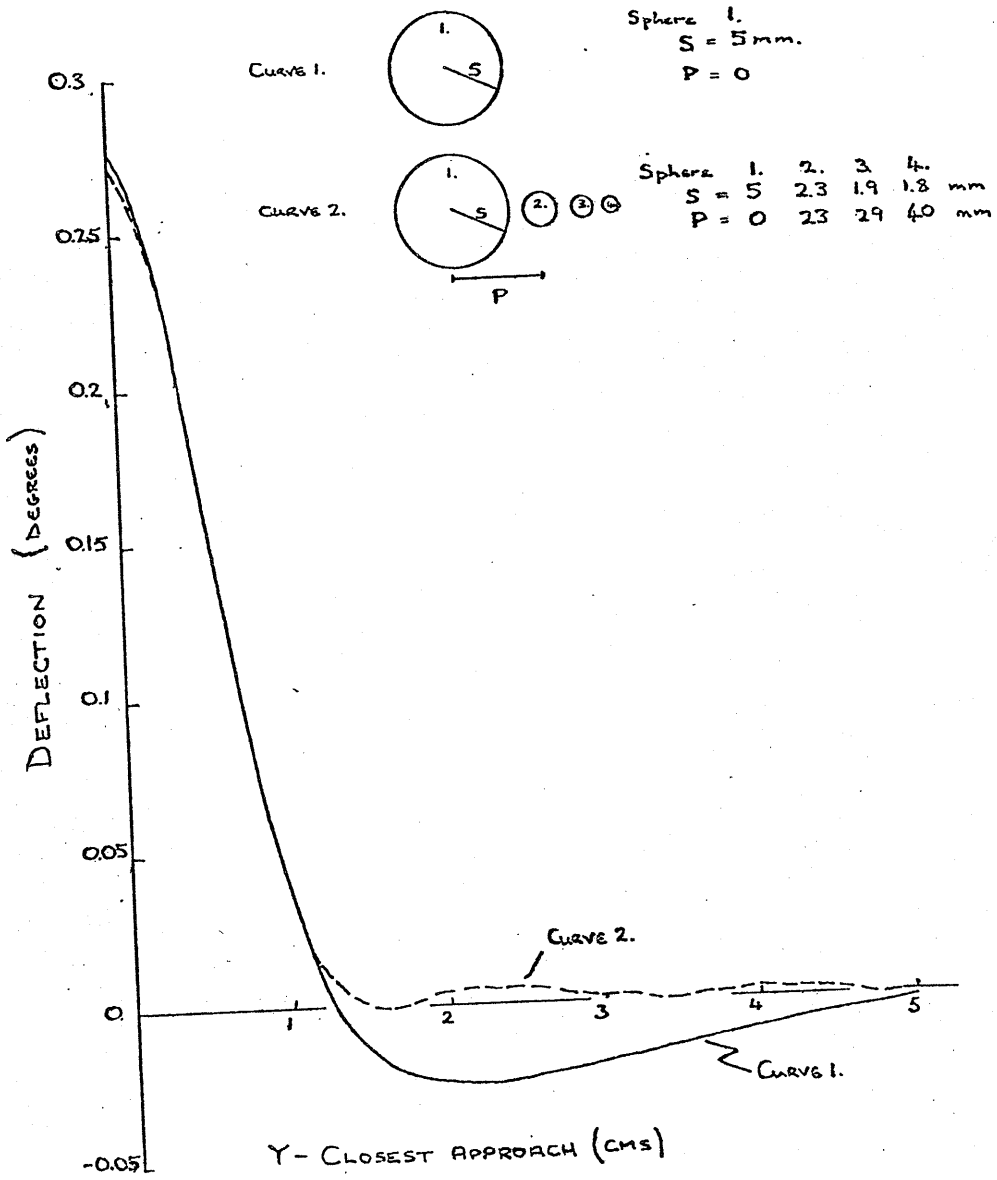

Figure 13. Deflection of proton orbit caused by the regenerator.

values of Z1. This causes the orbits to be distorted in the opposite direction from that required.

This negative effect is overcome by the addition of the secondary pairs of spheres as shown in Fig. 12a. The effect of these is added by first calculating the coordinates of the path of the protons with respect to the axes of each pair of secondary spheres using the subprogram LINE. MAGFLD is then used to calculate the field at each point, these are added to the value of BB (K) already obtained for that corresponding point. The deflection is calculated once the field of each set of spheres has been added to BB (K). The optimized design is shown as curve 2 in Fig. 13. The maximum deflection is only reduced by 2%, but now the deflection is approximately zero for Y greater than 14 mm.

2.2 Orbit Calculation

The second objective was to see how the perturbing fields would effect the orbits within the cyclotron. The set up, as explained previously, is a peeler in one hill region, the regenerator at the next hill such that their positions subtend 90° at the centre of the cyclotron.

The outline of this program is shown in Table 4 and reproduced in Appendix II. It is basically the same except that the protons now pass through the regenerator at an angle with respect to the x-axis, again the values of Z1 (K) are determined at 1 mm intervals along the path out to a value of 5 cm. The path is assumed straight, the deflection being added to the proton's path only after the proton has left the perturbing field.

The peeler field and the corresponding deflection it causes to the proton's path is calculated using the regenerator field and reversing

Table 4.

ORBIT CALCULATION

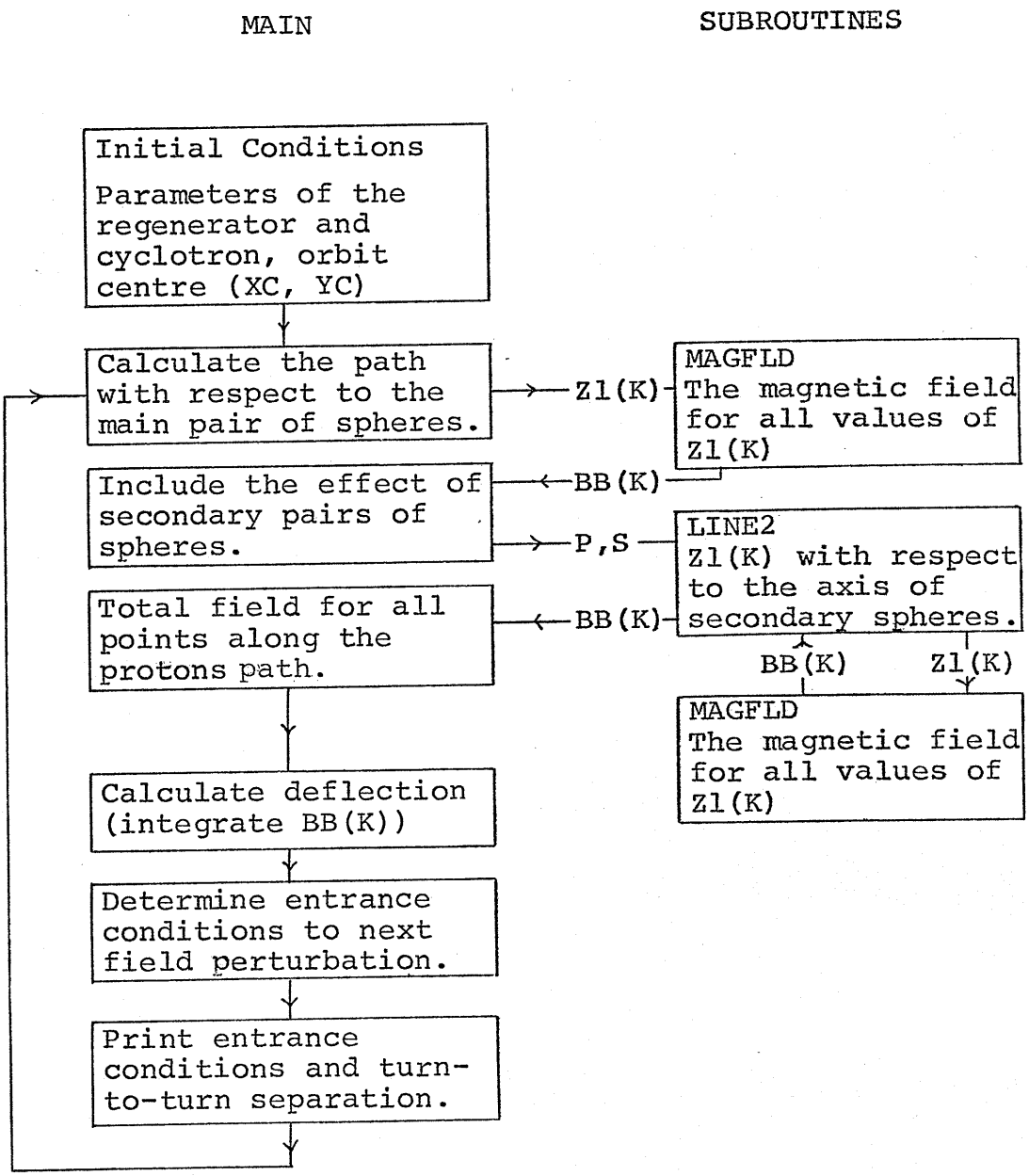

the deflection such that it is outward rather than inward. This is because the electrostatic deflection caused by the peeler would have a similar variation with Y as found for the magnetic deflection caused by the regenerator.

The initial conditions define the radius at which the regenerator and peeler are located and the centre of the proton orbit before it enters the perturbing field. The deflection to the orbit is calculated as the orbit passes through the peeler. Having added this deflection to the orbit the entrance conditions to the regenerator field are calculated, and the resulting deflection is added. The entrance conditions to the peeler are then found and this loop continues until the radius of the proton exceeds a defined limit.

In calculating the path of the protons between the two perturbing fields an average magnetic field is assumed; the variation in radius between hill and valley is neglected.

The results from this program using the regenerator design shown for curve 2 in Fig. 13 are given in Table 5. These results are as the proton orbit passes close to the central axis of the peeler and regenerator.

The table starts with the parameters for the 186th orbit since the proton entered the perturbing fields. The first set of values for each value of the orbit the exit conditions from the peeler, the second, from the regenerator. The parameter of interest is the separation of orbits between the peeler and regenerator, as can be seen, this has increased from 0.2 mm to a maximum value of 4.2 mm.

Table 5. Parameters of the proton orbits as they pass the central region of the regenerator field.

Orbit	Deflection from x-axis on leaving the perturbing field	Position of centre of rotation of the proton's orbit		Separation of neighbouring orbits
		x coordinate	y coordinate	
186.0	0.52563617 DEG	0.0050071 M	0.0049307 M	0.0011215 M
186.0	0.63029875 DEG	0.0050179 M	0.0060041 M	
187.0	0.64835401 DEG	0.0061784 M	0.0060160 M	0.0015967 M
187.0	0.79583776 DEG	0.0061979 M	0.0075837 M	
188.0	0.83247602 DEG	0.0079357 M	0.0076062 M	0.0023700 M
188.0	1.04022282 DEG	0.0079728 M	0.0099159 M	
189.0	1.10163429 DEG	0.0105051 M	0.0099587 M	0.0034837 M
189.0	1.34692631 DEG	0.0105653 M	0.0128438 M	
190.0	1.40843335 DEG	0.0134351 M	0.0129068 M	0.0041564 M
190.0	1.59086363 DEG	0.0134933 M	0.0151748 M	
191.0	1.66561647 DEG	0.0158935 M	0.0152394 M	0.0033889 M
191.0	1.72795457 DEG	0.0159298 M	0.0164882 M	
192.0	1.87133028 DEG	0.0178623 M	0.0165479 M	0.0023640 M
192.0	1.79485671 DEG	0.0178803 M	0.0171326 M	
193.0	2.04660099 DEG	0.0195418 M	0.0171895 M	0.0017978 M
193.0	1.82114097 DEG	0.0195481 M	0.0173898 M	
194.0	2.20612183 DEG	0.0210719 M	0.0174463 M	0.0015516 M
194.0	1.82380097 DEG	0.0210711 M	0.0174215 M	

3. CONCLUSION

This study has shown that the use of an electrostatic peeler and magnetic regenerator makes possible an increase in the turn-to-turn separation of the proton orbits in the Manitoba cyclotron from 0.2 to 4.2 mm. This separation is large enough to enable extraction of the accelerated beam from the cyclotron using an electrostatic deflector with a high efficiency.

The next step in this study would be to determine the extraction efficiency which could be obtained using this system. Owing to the approximations made in these programs the efficiency could only be calculated to first order. In particular the effect of neighbouring spheres is ignored in calculating the magnetic moment induced in that pair of spheres for which the magnetic field is being determined. Also the hill-valley sectors are neglected in calculating the orbit parameters.

CHAPTER III

MULTIWIRE PROPORTIONAL COUNTER WITH DELAY LINE READOUT

1. INTRODUCTION

Multiwire proportional counters have proved to be a very powerful tool in both nuclear and particle physics experiments. The principles on which these counters are based are now well understood (Charpak, 1970; Palladino and Sadonlet, 1974) and their capabilities have resulted in their wide use. These properties are:

i) large solid angle

ii) high count rates

iii) high resolution for both coordinates of the particle trajectory through the detector

iv) high efficiency

The major prohibiting factor in their use has been their cost, it being necessary to have an amplifier on each wire and an elaborate set up to determine on which wire the pulse was induced. Two techniques have successfully been applied to reduce costs, however both suffer from reduced performance in one or more of the above properties. One method has been the development of the drift chamber (see Pogson, 1976 and references therein), however this detector is only capable of locating a single coordinate of the particle's path.

A second technique is the incorporation of delay lines into both anode and cathode planes (D. Lee, 1972, 1973, 1974). The cathode is wound as a flattened helix around the anode plane, the latter acts as the ground plane resulting in the helix acting as a delay line. A pulse induced on the cathode travels in both directions away from the site of the initial avalanche. The difference in arrival time of the pulse at either end of the helix is proportional to the position of the initial

pulse giving the coordinate along the axis of the helix. The anode wires give the second coordinate, each wire is tapped directly, at regular intervals onto a delay line, thus permitting the pulse to travel from the anode wire onto the delay line in either direction away from the junction. Again the time difference is measured between the arrival of the pulse at either end of the delay line, this being proportional to the initial position of the pulse. A schematic diagram of this set up is shown in Fig. 14.

Clearly the cost is considerably reduced, just two amplifiers and a Time to Amplitude Convertor (TAC) are required for each coordinate. However this design is not capable of particle identification and some of the designs have long dead times limiting count rates.

I have designed and tested such a detector based on that described by D. Lee (1973, 1974). The parameters were chosen with a view to using the detector in a radiative capture experiment being undertaken in the laboratory using the recently established neutron beam line. In that experiment a deuteron from $p(n,d)\gamma$ will be emitted with a cone of half angle between 3 and 5° for neutron energies between 20 and 50 MeV, thus the wire chamber required should have a small cross section but a high position resolution.

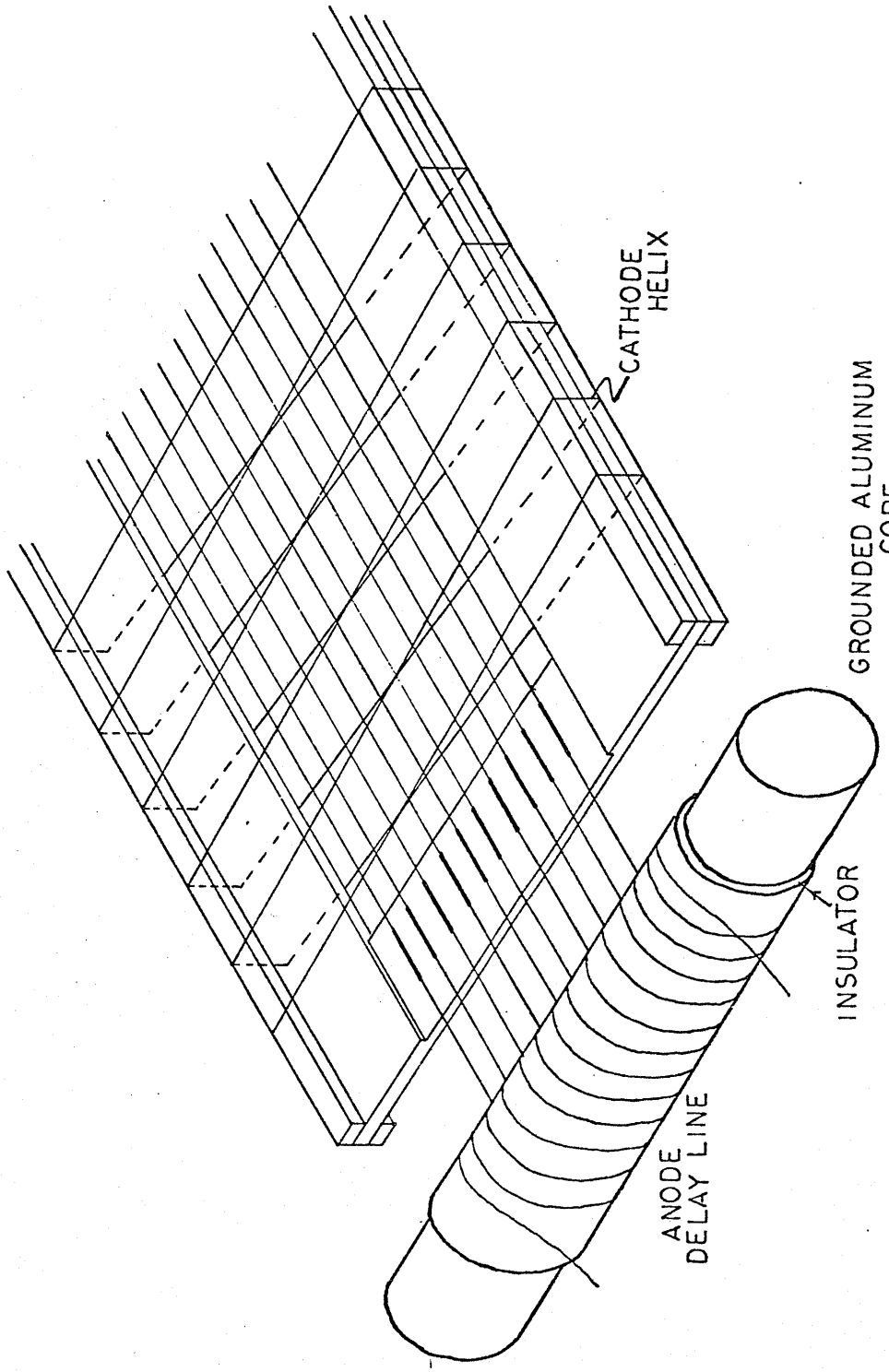

Figure 14. Monofilar helical cathode and anode delay line.

2. PRINCIPLES

2.1 The Multiwire Proportional Counter

Many detailed analyses have been carried out on the operation of these detectors (eg. Palladino and Sadonlet, 1974). A brief summary of the processes involved and the basic design follows:

The ions pass through a region of high electric field which exists between two parallel planes of fine wires orientated at right angles to one another. The ions leave a trail of ionized atoms in the gas, these are accelerated by the electric field causing a charge separation. The anode is made of very thin wire, normally 10 - 20 μm, the field around each wire is cylindrical, thus proportional to 1/r. Within a few diameters of these wires the electrons gain sufficient energy to cause further ionization resulting in the avalanche effect. Argon is the most commonly used gas,predominantly due to its abundance of electrons,because it is inert and it has the highest probability for ionization following inelastic electron collison. Higher valent atoms, in the form of molecules tend to excite rotational and vibrational bands which do not add to the gas amplification. A second gas is normally added to act as a quenching agent. Photons are emitted through the photoelectric effect caused by electron and ion collision with atoms and the wires, these cause further ionization and can cause the pulse to have a long fall time. The addition of a gas of larger molecules absorbs the photons more readily decreasing the fall time.

The separation of the ions produced by the projectile and in the avalanche induce pulses on those wires in both anode and cathode planes in the vicinity of the avalanche. Thus by identifying the wire from which the pulse originates the coordinates of particle's trajectory can be obtained.

2.2 The Cathode Delay Line

Two types of helix have successfully been incorporated into multi-wire proportional counters by D. Lee et al. The first is a single continuously wound flattened helix forming both cathode planes on either side of the anode plane (Fig. 14). This is described as a monofilar helical cathode. The principles, construction techniques and results are given by D. Lee (1973). The second is a double helix, the first is grounded at each turn, the second is wound between the first in the same plane, with the same pitch such that each turn lies between two consecutive turns of the grounded helix (Fig. 15). This is described as a bifilar helix. The chamber, its principles and parameters are given by D. Lee (1972). The first has a high impedance, however this varies with frequency which means the delay line cannot be perfectly terminated with a pure resistance. This fact along with the high impedance which results in low attenuation causes problems with reflections, producing a long dead time. However this set up has a higher resolution than the bifilar helix since alternate wires in the cathode of the latter are grounded and thus are not capable of determining the position of a pulse.

The effect of these grounded wires is to make the helix behave as a parallel transmission line for which theory is well understood (Gray, 1957), the impedance is low and constant with frequency, it can be terminated resistively, thus there are no reflections. However the low impedance causes high attenuation making this method impractical for large chambers unless the cathode pulse is tapped at regular intervals and separate time difference spectrum taken for each region.

The monofilar chamber was chosen for the radiative capture experiment because of its higher resolution. The problem of its long

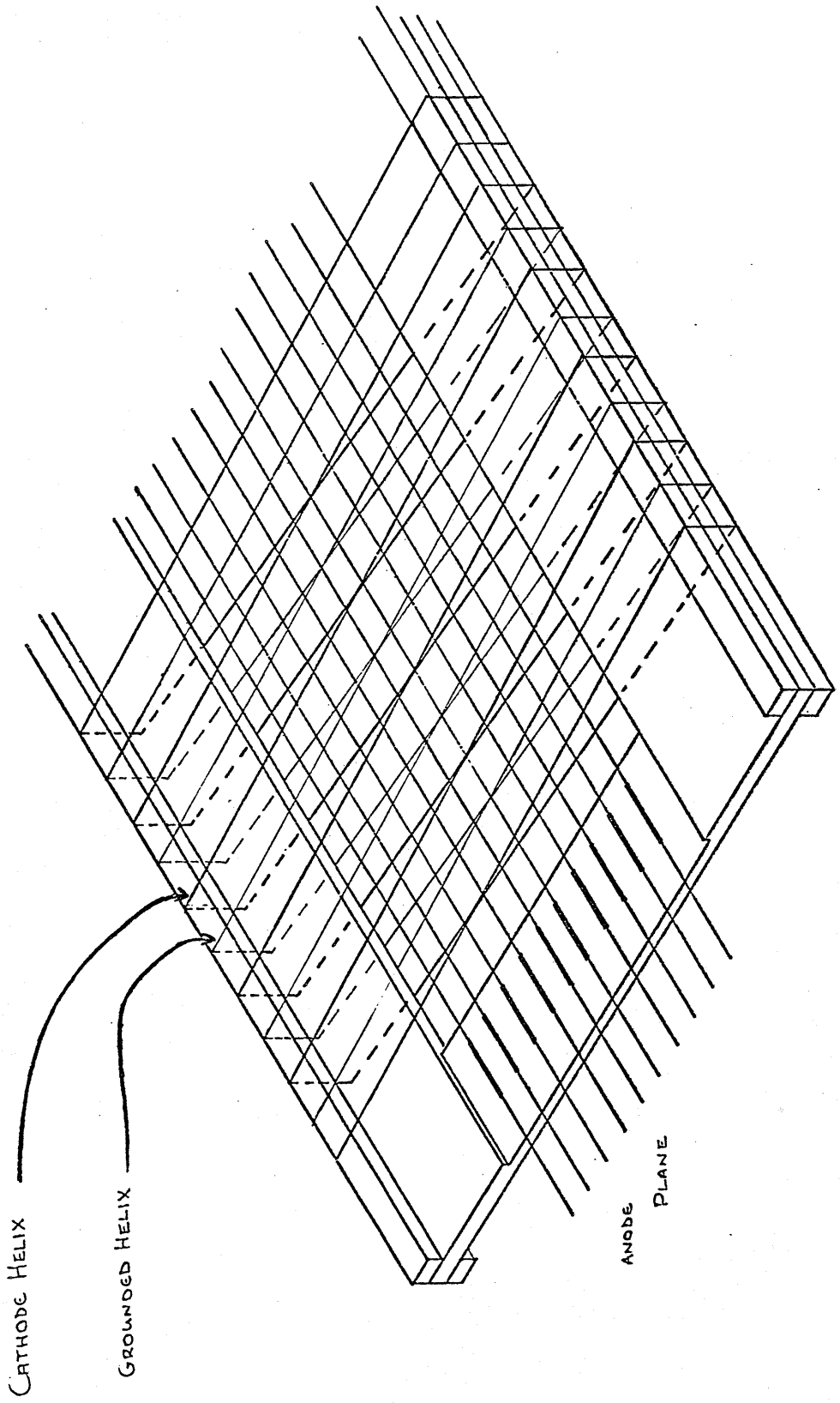

Figure 15. Bifilar helical cathode.

dead time is not anticipated to be a problem . The chamber described by D. Lee (1973) has a dead time of 5μs giving allowed count rates up to 10^4 s^{-1}. Also with suitable choice of parameters the attenuation should be increased, decreasing the number of reflections.

D. Lee (1973) derives the parameters for a monofilar cathode helix by using the sheaf helix model (Watkins 1958). The two cathode planes are assumed to be infinite planes at $x = \pm a$ conducting only in the direction parallel to the wires, ie. at an angle ψ to the z axis (Fig. 16). The ground plane at $x = 0$ conducts only along the y axis and the enclosing grounded planes at $x = \pm b$ conduct in all directions. Solving for the field components from the relevant boundary conditions, a dispersion relation is obtained, then the charactertistic impedance is derived as a function of the frequency of the waves propagating in the z direction. This is:

$$Z_o = \sqrt{\left(\frac{\mu_o}{\varepsilon_o}\right)} \frac{1}{2kw} \sin \gamma a \, (\cosh \gamma a - \coth \gamma b \sinh \gamma a)$$

The angle ψ has been replaced by the expression

$$\cot \psi = 2w/p$$

where p is the pitch and w the width of the cathode helix, $k = \omega/c$ and γ is a wave number related to the wave propagation along the wire. From this expression the impedance with respect to frequency can be derived for any set of parameters of the helix. Fig. 17 gives this function for various values of a/p and w with a conducting shield at infinity while Fig. 18 gives a reduction factor as a function of frequency for various positions of the outer shield. Since the attenuation along the delay line is given by the factor $\exp(-R/2Z_o)$ where R is the series resistance of the delay line. A constant value of Z_o is required for a

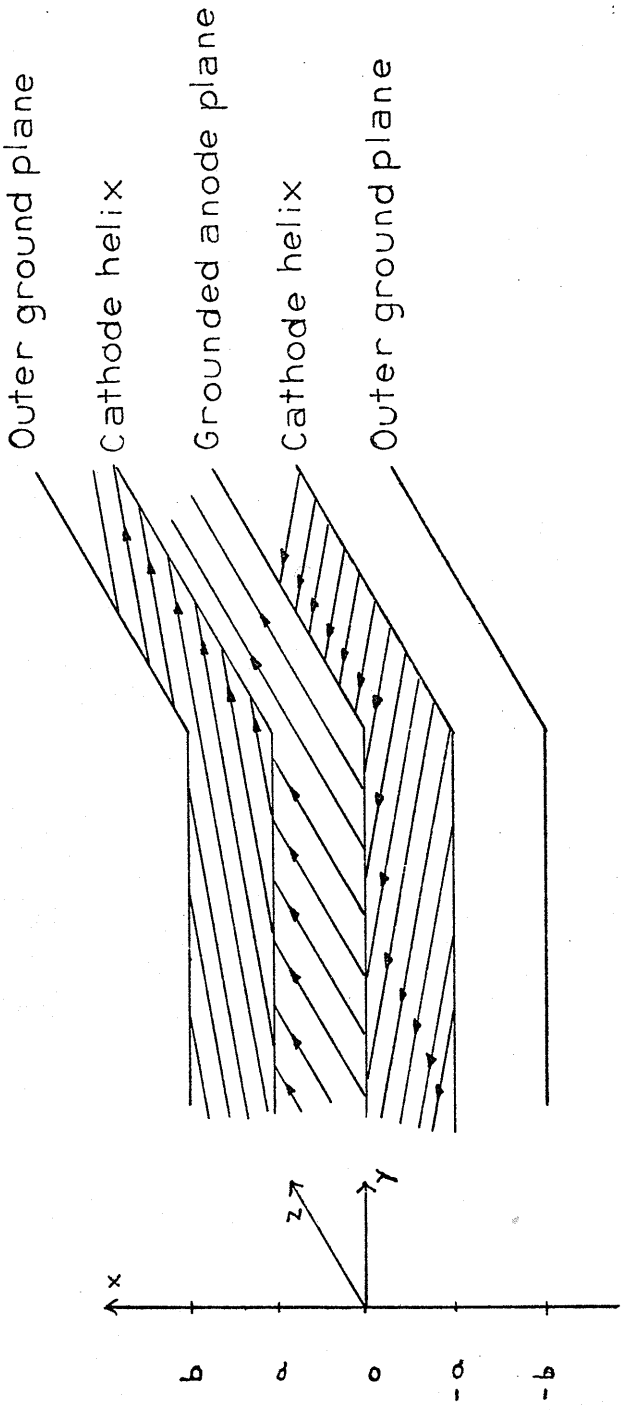

Figure 16. Diagram showing approximations made in using sheaf helix model for the monofilar helical cathode. (D. Lee, 1973)

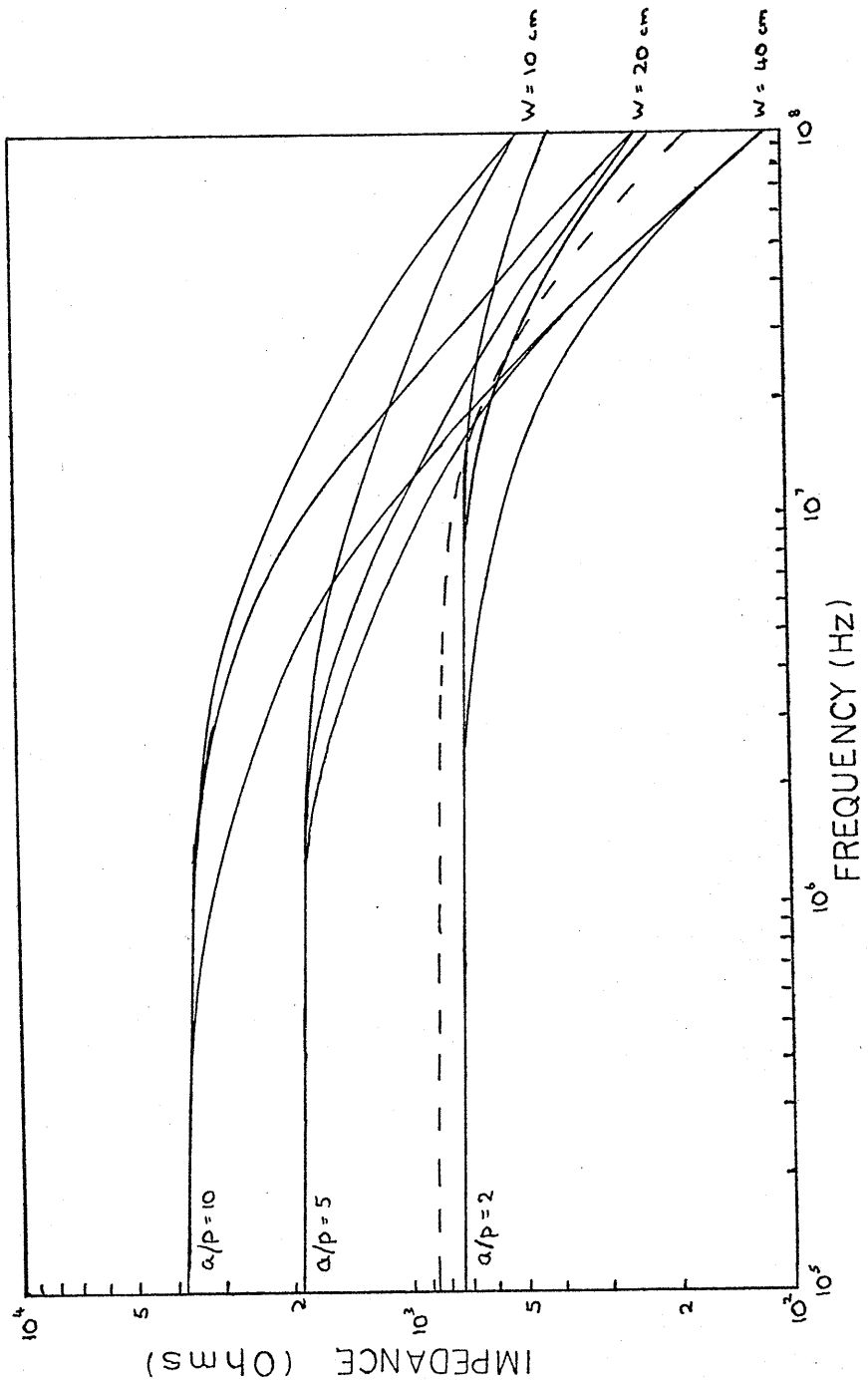

Figure 17. Impedance as a function of frequency for the monofilar helix. (D. Lee, 1973)

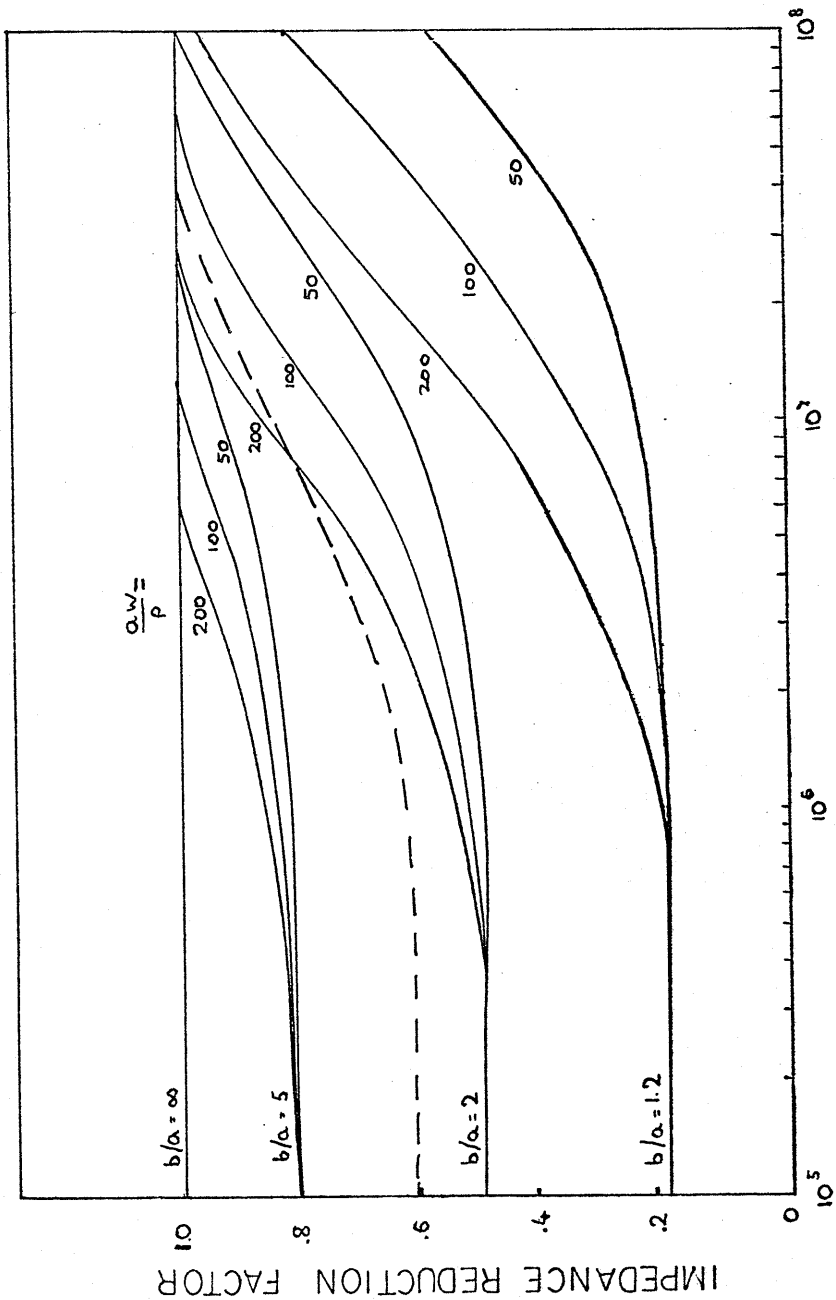

Figure 18. Impedance reduction factor. (D. Lee, 1973)

constant attenuation with respect to frequency. This is essential for the optimum position resolution in the cathode plane since the position is located by timing taken from the leading edge of the pulse induced on the anode. In order to obtain the minimum variation in pulse rise time a narrow chamber is required with a low value for a/p. Also the ratio b/a should be as large as possible.

2.3 The Anode Delay Line

The anode is incorporated into a delay line by tapping each wire to consecutive turns on a helical delay line (see Fig. 14). This delay line is based on that described by D. Lee (1974). A thin insulator, thickness a is placed between the grounded aluminium core and the helix, this gives a low value for the ratio a/p. Thus, although the helix is again approximated by a flattened helix, the impedance is a constant with frequency, being given by

$$Z_o = 377\ a/p \quad \text{Ohms}$$

Using both mylar and polythene suitable delays were obtained with minimal degradation in pulse rise time. However this delay line has been replaced by one formed from double sided copper etching board. The upper surface is etched to have a continuously zigzagged line, each anode wire being tapped at regular intervals to the line Fig. 19. The lower surface is untouched and acts as the ground plane, the insulator on which the copper is plated is thin, so the delay line has a constant low impedance thus pulses propagate with no change in rise time. This delay line was obtained from Chris Morris* from LAMPF.

---

*Private Communication.

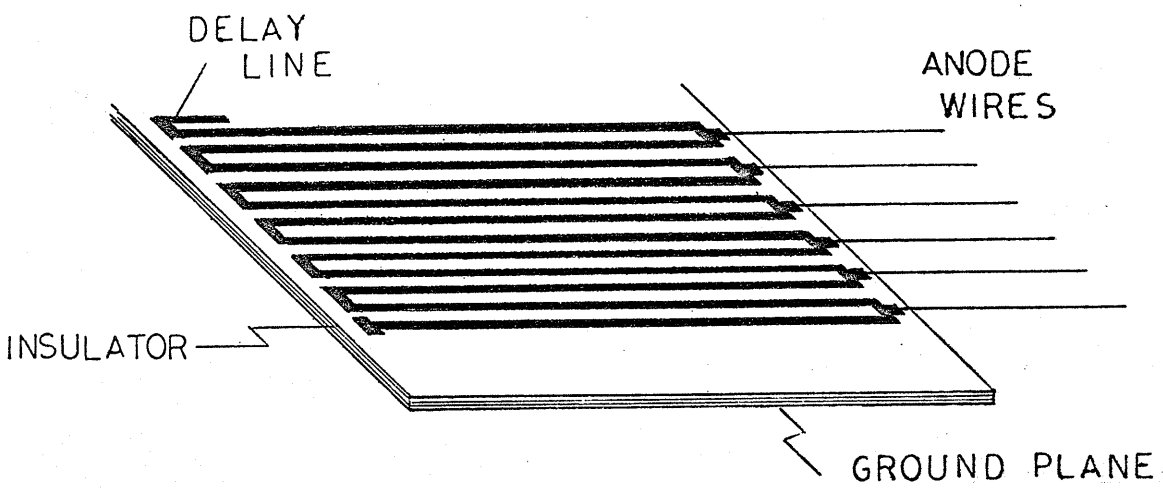

Figure 19. Copper etched anode delay line.

3. CONSTRUCTION DETAILS

G10, a fibre glass reinforced epoxy board, was used for all supporting frames in the wire chamber. This material has been shown to be one of the most suitable particularly because it has a high resistance to surface breakdown in high electric fields.

The anode plane and delay line were mounted on a single G10 frame 10" x 7½" x 1/8" with a 5¼" x 3½" portion removed at one end across which the anode wires were strung. Copper contacts spaced at 2 mm intervals were etched using a master copy shown in Fig. 20. The pointed ends of the contact were necessary to ensure regular spacing of the anode wires, this being vital to produce a symmetric cylindrical electric field around each wire, see p. 214 Charpack(1970). These contacts were mounted in recessed platforms in the frame along the two 5¼" sides of the gap. The delay line was mounted on the remaining portion of the frame, its axis parallel with the contacts.

The anode wires were strung across the gap, soldered to the contacts on either side and to consecutive turns of the delay line. 12 μm gold plated tungsten wire was used for the anode. Tests showed the wire to have a breaking strain of 30 gms tension. Calculations showed that a maximum change in tension of 7 gms would result from any conceivable temperature change. Thus each wire was soldered with 12 gms tension so that it would never become slack nor would it break. All attempts were made to keep the wire clean during construction, particularly the wire was never touched, a clean and even surface being necessary to avoid breakdowns.

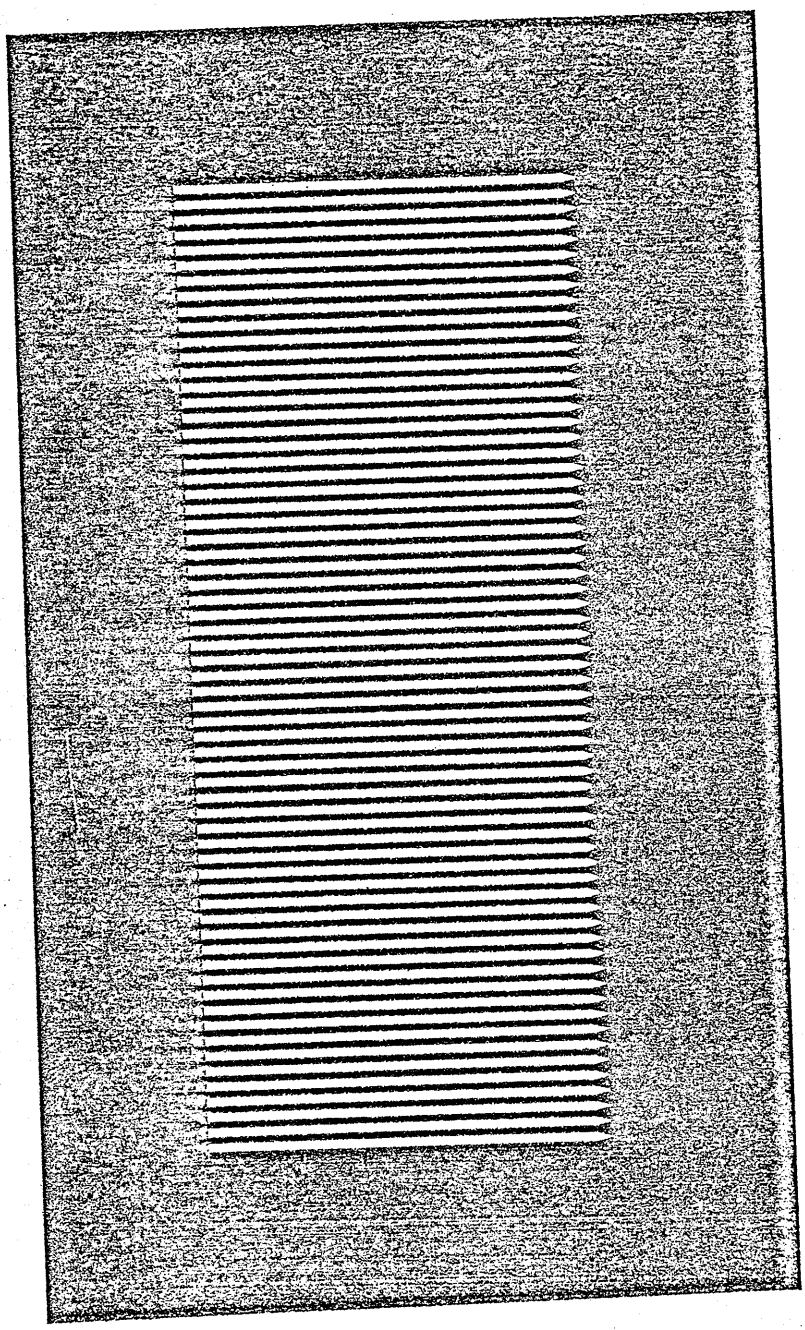

Figure 20. Master copy used to make copper contacts for anode wires.

The anode plane acts as a ground plane for the cathode helix, however this plane is not complete, it was extended using 2 Aluminium foil strips, placed on either side of the gap parallel to the anode wires and grounded to the anode plane. In order to avoid any chance of surface breakdown the anode wires were not strung less than ¼" from the edge of the frame. A second frame, 6" x 7½" x 1/8" with a 5¼" x 3½" gap, was placed over the first in order to separate the two cathode planes equally from the ground plane. The cathode delay line was wound with 50 μm copper plated tungsten with a pitch of 1.3 mm. The wire chamber was enclosed in a box made from G10 frames, the windows being covered by grounded Aluminium foil.

The parameters discussed in Sec. 2.2 which determine the impedence of the cathode helix were chosen to obtain minimal degradation of the pulse rise time. The values are

$$a/p = 2.5$$

$$w = 29 \text{ cm.}$$

This dependence is shown in Fig. 17 as a dashed line, similarly the impedance reduction factor is determined by b/a and aw/p, the values are

$$b/a = 3$$

$$aw/p = 72 \text{ cm.}$$

This dependence is shown as the dashed line in Fig. 18. This gives a low impedance which should result in high attenuation, however since the helix is only 3" long this is not a problem and with a high attenuation the number of reflections will be reduced decreasing the dead time from that reported by Lee (1973) for a larger chamber.

The gases used were Argon and CO_2. The latter acts as the quenching agent and was chosen following a study by A. Stetz and V. Perez-Mendez (1973). They found that CO_2 was preferable to CH_4. A mixture of 70% Argon, 30% CO_2 was found to give maximum gain and faster pulses with the least flutter Each gas was fed through filters made from fine molecular sieve and glass wool in order to remove water vapour, particles and oil. The gas mixture was controlled through two flow valves, a continuous flow being used in the order of 50 cc/min., this results in the chamber being at a pressure slightly above atmospheric.

4. TESTING OF THE CHAMBER

The delay and transmission properties of both anode and cathode have been measured using a pulse generator. The anode delay line gives a 48 ns delay (Fig. 21a) resulting in a 1.3 ns delay between consecutive junctions of the delay line with anode wires. The delay line has an impedance of 80Ω . A pulse transmitted through the delay line shows no reflections or degradation of the pulse rise time. The attenuation along the delay line is 0.4.

The cathode delay has been measured as 70ns or 9.2 ns /cm. A pulse with 20 ns rise time shows negligible degradation in rise time after passing along the delay line. The reflections are reduced from the 4 shown by Lee (1973) to a single reflection 1/10 times the original pulse (Fig. 21b). This high attenuation is a result of the low impedance, approximately 580 Ω. The attenuation of pulses with a shorter rise time than 20 ns increases rapidly, this is a result of the non-linear frequency dependence of the impedance, see Fig. 17 and 18.

Provided sharp pulses are induced on the cathode and anode by the ionizing radiation and the chamber noise level is low, these results suggest that the delay in the cathode helix is sufficient to give high position resolution and the delay in the anode is large enough to resolve each wire. Also the lack of reflections observed on the input pulse compared with Lee (1973) suggests the dead time should be considerably shorter than the 5 μs for his larger chamber.

A Na^{22} gamma source has been used to test the chamber, the electronics set up used to measure the cathode resolution is shown in Fig. 22, an identical arrangement is used to test the anode.

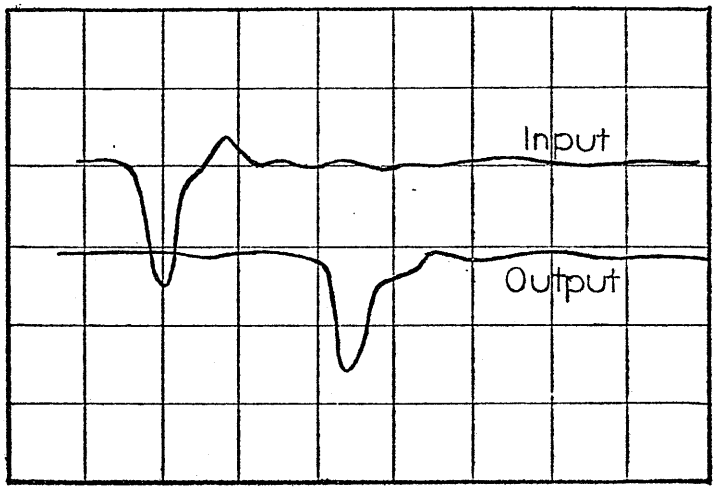

Figure 21a. Transmission of pulses down anode delay line.
Horizontal scale: 20 ns/cm.
Vertical scale - upper trace: 0.5 volts/cm.
lower trace: 0.2 volts/cm.

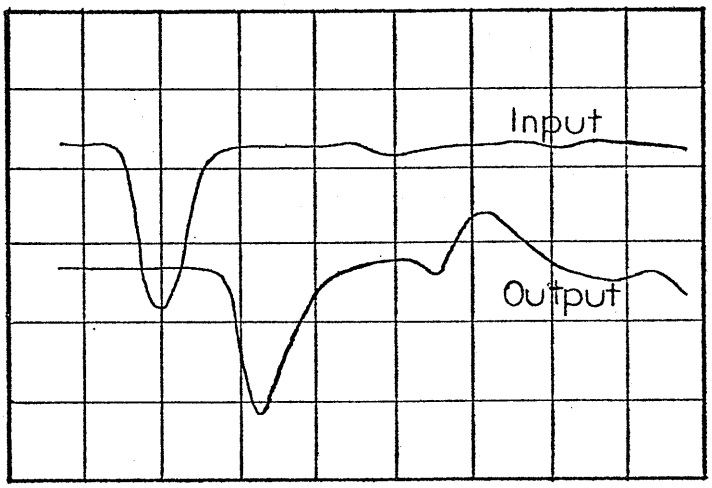

Figure 21b. Transmission of pulses through cathode helix.
Horizontal scale: 50 ns/cm.
Vertical scale - upper trace: 0.5 volts/cm.
lower trace: 0.1 volts/cm.

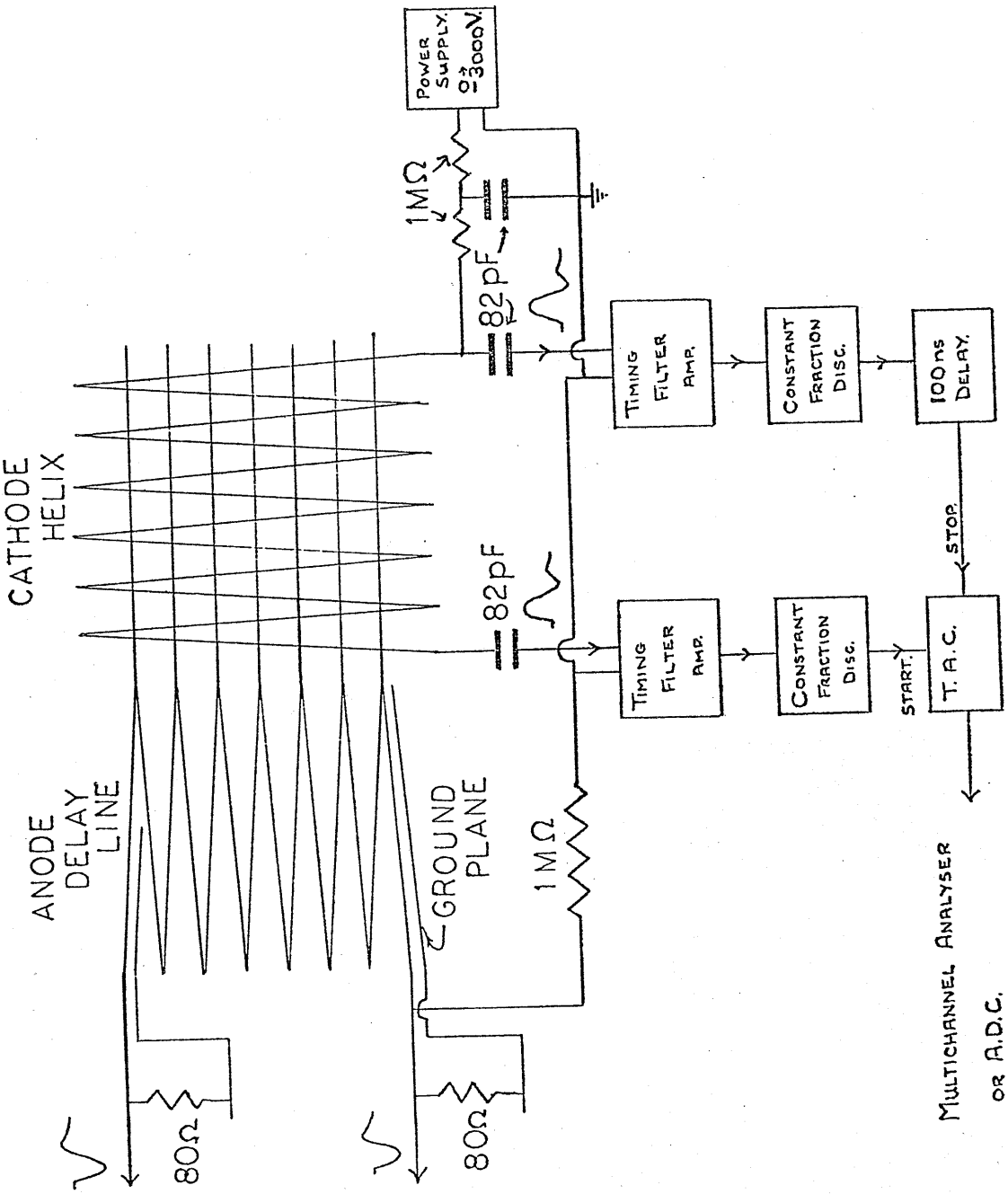

Figure 22. Electronics set up for wire chamber.

With the gas mixture set at 70% Argon, 30% CO_2, pulses from the gamma rays are observed above 2500 volts. The pulses increase in size with voltage, however breakdown occurs in the chamber at 2800 volts. With an increased concentration of CO_2 this breakdown voltage increases, with 50% CO_2 the breakdown occurs at 2880 volts.

Typical anode pulses have a rise time between 10 and 15 ns, the fall time is of the order of 20 ns, the cathode pulses have a similar rise time, the fall time is typically 30 - 60 ns. These times depend on the mixture of the two gases and on the operating voltage. At present the pulses are not smooth but show some jitter, this is partly due to jitter on the raw pulses induced on the anode or cathode by the avalanche in the gas and partly due to noise pick up from external sources and from the amplifier. To date the best timing obtained from the Constant Fraction Discriminators gives pulses with a jitter of 1 - 2 ns.

The two causes of this effect, i.e., the gas and external noise are under investigation. The relative proportions of Argon and CO_2 will be optimized or better quenching agents found, possibly isobutane as used by D. Lee et al, and the pick up of external noise reduced by improved shielding.

Despite the jitter time difference spectrum have been taken for both anode and cathode planes. With the stop pulse to the TAC delayed by 100 ns all start and corresponding stop pulses from both anode and cathode come within 200 ns. When the chamber is in a uniform flux of gamma rays the time difference spectrum from the cathode pulses shows a uniform plateau, the edges corresponding to pulses from the edge of the helix. The width is 140 ns which corresponds to double the delay of the helix.

The anode delay line shows a plateau 100 ns wide with 4 narrow peaks above this plateau. However to resolve each anode wire 56 peaks,

one for each anode wire, would be expected. The reason for the inability to resolve pulses from each wire is due to the jitter on the pulses. The 4 peaks show that some anode wires are more active than others, this is because the anode wire spacing is not uniform. This can only be overcome by greater care in soldering and aligning the anode wires on the contacts or by using an improved technique to accurately space the wires, possibly by adapting a mill to space the wires across the anode. It is possible that the breakdown which occurs above 2800 volts is due to some anode wires being too close, a uniform spacing would then allow a high voltage between anode and cathode decreasing the jitter on the pulses.

CONCLUSION

Clearly the major problem at present is the lack of uniformity in the anode wire spacing. Improvement in the technique for aligning these wires will be the next improvement implemented. Then it is expected that by optimizing the gas mixture the jitter in pulses will be reduced sufficiently to enable good stability and high resolution to be achieved. Once the jitter has been removed the anode delay is sufficient to resolve each wire and the cathode delay is large enough to achieve a resolution in the same order as that quoted by Lee (1973), that is 0.33 mm FWHM.

A further extension of this design is to incorporate three detectors within a single gas box. This design may be suitable and necessary for the radiative capture experiment mentioned earlier. A multiwire proportional counter with delay line readout would be positioned at the entrance window and another at the exit window of a suitably designed drift chamber. The latter would enable particle identification to be made while the two multiwire proportional counters add the ability to trace the trajectory of each particle. The advantage of enclosing the three components in one complete system is that the number of windows in the path of each projectile is reduced, thus decreasing energy loss and the production of background deuterons.

CHAPTER IV

A MECHANISM FOR DIPROTON PRODUCTION IN THE SUN AND ITS EFFECT ON THE HYDROGEN BURNING CYCLE

1. INTRODUCTION

In a study of the reaction $^{3}He(^{3}He,2_{p})^{4}He$ our calculations show that diproton production is the dominant inelastic channel for energies below the Coulomb barrier. The effect of this hypothesis and the experimental results of Slobodrian (1975) on the hydrogen burning cycle in the sun have been considered. Our results from this study are described in detail in the two papers which follow.

2.1 "Neutron tunnelling as a Mechanism for Diproton Production in the Sun"

J.S.C. McKee and C. Randell

"Second International Conference on Clustering Phenomena in Nuclei"

University of Maryland

April 21 - 25, 1975

2.2 "Diproton Production, and its Influence on the Hydrogen Burning Cycle"

J.S.C. McKee and C. Randell

Nuclear Physics (1976) A 260 p 344 - 348

2. REPRINTS

2.1 Neutron Tunnelling as a Mechanism for Diproton Production in the Sun

J.S.C. McKee and C. Randell
Cyclotron Laboratory, Department of Physics
University of Manitoba
Winnipeg, Canada

The neutron tunnelling model is shown to indicate that diproton production can be the dominant inelastic channel for the $^3He(^3He,^4He)^2He$ reaction in the solar interior.

The antibound singlet S-state of two protons, described variously as the diproton or ^2He, has attracted much interest during recent years. It is created with considerable probability in particle transfer reactions involving light nuclei, particularly those which leave two protons in a final state in which the cross sectional area of their interaction is small as compared with their scattering cross section. The possibility of the existence of a source of diprotons in the solar interior is examined in some detail in this paper.

In the consideration of reactions by which diprotons might be created in the sun, it is possible immediately to reject the fusion reaction $p+p\rightarrow{}^2He$ on a number of grounds.

A much more probable source of diprotons is to be found in the reaction $^3He+^3He\rightarrow{}^4He+p+p$ in the proton chain of hydrogen burning in the sun. The problem in this case is to identify a production mechanism at low energies which can fill the role of $\ell=0$ nucleon transfer at higher energies (1). Two comparatively recent publications are relevant to this problem. Firstly, May and Clayton (2) have adopted the neutron tunnelling model of Breit and Abel (3) to show that at energies below the Coulomb barrier the diproton may be the predominant final state from the ^3He-^3He reaction. Dwarakanath and Winkler (4) tend to disagree, as the energy dependence, obtained by May and Clayton (2) for the function S(E), when $S(E)=S_o+S_o' E_{cm}$, gives a value for S_o' at low energies which, although negative as observed experimentally, is nevertheless too small in absolute terms to fit the data.

Secondly, a comparison of the reactions (A) $^3H(^3He,^4He)^2H$ and (B) $^3He(^3He,^4He)^2He$ at 16.0 MeV (5) and below 1.5 MeV (6) centre-of-mass energy, shows that isospin conservation is good in these reactions to within a few per cent in overall accuracy. Conservation of isospin of course requires that the nuclear cross section for production of the diproton (B) has twice the magnitude and the same angular distribution as

for reaction (A). This fact enables us to predict the cross section for reaction (A) under the assumption that neutron tunnelling from the triton to the helion is the dominant mechanism by which reaction (A) can proceed below the Coulomb barrier. We have closely followed the treatment of May and Clayton (2), assuming isospin conservation, and adjusting the spectroscopic factors and Coulomb terms appropriately. Good agreement is obtained with the experimental data of Kuhn and Schlenk (7) for energies up to 700 keV (see Figure 1). In the vicinity of the Coulomb barrier however, the agreement between the model and the experimental data deteriorates, presumably because of the increased probability of alternative reaction mechanisms. This result tends to suggest that not only is diproton production important below the Coulomb barrier but that it is the dominant mechanism by which the reaction between two helions can proceed at such energies. The β-decay rate of ^{2}He is clearly relevant to any calculations of the flux of solar neutrinos. Further measurements of this quantity both experimental and theoretical are urgently required.

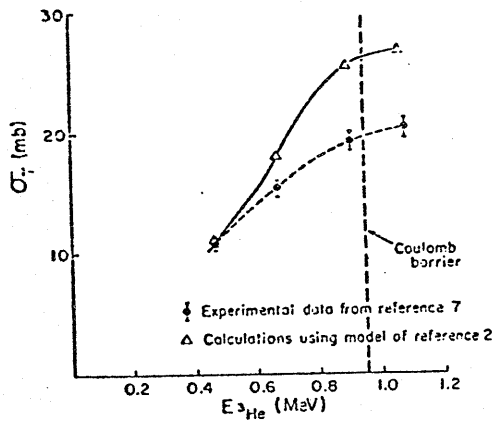

Figure 1.

1. See for example, R.J. Slobodrian, J.S.C. McKee, W.F. Tivol, D.J. Clark and T.A. Tombrello, Phys. Letts. 25B, 19 (1967).
2. R.M. May and D.D. Clayton, Astrophys. Jour. 153, 855 (1968).
3. G. Breit and M.E. Ebel, Phys. Rev. 103, 679 (1956).
4. M.R. Dwarakanath and H. Winkler, Phys. Rev. C4, 1532 (1971).
5. W.J. Roberts, E.E. Gross and E. Newman, Phys. Rev. C9, 149 (1974).
6. K.S. Nam, G.M. Osetinskii and V.A. Sergeev, Yad. Fiz. 10, 705 (1969).
7. B. Kuhn and B. Schlenk, Nucl. Phys. 48, 353 (1963).

2.2
1.B

Nuclear Physics A260 (1976) 344–348; © *North-Holland Publishing Co., Amsterdam*
Not to be reproduced by photoprint or microfilm without written permission from the publisher

DIPROTON PRODUCTION, AND ITS INFLUENCE ON THE HYDROGEN BURNING CYCLE

J. S. C. McKEE and C. RANDELL

Cyclotron Laboratory, Department of Physics, University of Manitoba, Winnipeg, R3T 2N2, Canada

Received 31 July 1975
(Revised 17 December 1975)

Abstract: Calculations using the neutron tunnelling model indicate that diproton production is the dominant mechanism by which the ^{3}He(^{3}He, ^{4}He)2p reaction can proceed below the Coulomb barrier. The implications of this result are discussed in relation to the hydrogen burning cycle in the sun.

The antibound singlet S-state of two protons, described variously as the diproton or ^{2}He, has attracted much interest in recent years. It is created in particle transfer reactions involving light nuclei, particularly those which leave two protons in a final state in which the cross sectional area of their interaction is small compared with their scattering cross section. The possibility of the existence of a source of diprotons in the solar interior is investigated in some detail in this paper, and conclusions are drawn as to the likely relevance of such a source to the solar neutrino problem.

In the consideration of reactions by which diprotons might be created in the sun it becomes possible to reject the fusion reaction $p+p \rightarrow {}^2He$. From examination of the limiting case of two protons moving in the same direction with low relative momentum, in the same region of a Maxwellian velocity distribution, it is clear that such particles cannot overcome the Coulomb barrier between them for realistic particle velocities.

A much more probable source of diprotons is to be found in the reaction $^3He+{}^3He \rightarrow {}^4He+{}^2He$ because of the known presence of the reaction $^3He+{}^3He \rightarrow {}^4He+p+p$ in the proton chain of hydrogen burning in the sun. The problem in this case is to identify a production mechanism at low energies which can fill the role of $l = 0$ nucleon transfer at higher energies [1]). Two comparatively recent publications are relevant to this problem. Firstly, May and Clayton [2]) have adopted the neutron tunnelling model of Breit and Abel [3]) to show that at energies below the Coulomb barrier the diproton may be the predominant final state from the ^{3}He-^{3}He reaction. Dwarakanath and Winkler [4]) tend to disagree, as the energy dependence obtained by May and Clayton [2]) for the function $S(E)$, where $S(E) = S_0 + S_0' E_{c.m.}$, gives a value for S_0' at low energies which, although negative as observed experimentally, is nevertheless too small in absolute terms to fit the data in the region of the Coulomb barrier.

Secondly, a comparison of the reactions (a) ^{3}H(^{3}He, ^{4}He)^{2}H and (b) ^{3}He(^{3}He, ^{4}He)^{2}He at 16.0 MeV [ref. [5])] and below 1.5 MeV [ref. [6])] c.m. energy, shows that isospin conservation is good in these reactions to within a few per cent in overall accuracy. Conservation of isospin of course requires that the nuclear cross section for production of the diproton (b) has twice the magnitude and the same angular distribution as for reaction (a) [ref. [5]) and references therein]. This fact enables us to predict the cross section for reaction (a) under the assumption that neutron tunnelling from the triton to the helion is the dominant mechanism by which reaction (a) can proceed below the Coulomb barrier. We have closely followed the treatment of May and Clayton [2]) in this calculation, assuming isospin conservation, and adjusting spectroscopic factors and Coulomb terms appropriately. The differential cross section for the reaction is written in the form

$$\frac{d\sigma}{d\Omega} = \frac{M_i M_f}{4}\frac{k_f}{k_i}(S_i S_f N_i^2 N_f^2)|C(\eta_i)|^2|C(\eta_f)|^2|B|^2|I(\theta)+I(\pi-\theta)|^2,$$

the angle-independent term B being defined by the equation

$$B = \exp[\eta_i\phi_1+\eta_f\phi_2+i(\eta_i+\eta_f)\psi_1+i(\eta_f-\eta_f)\psi_2],$$

and the angle-dependent term $I(\theta)$ by

$$I(\theta) = \frac{4\pi}{\mu(\gamma^2+\Delta^2)}e^{-i\eta_i\ln(\gamma^2+\Delta^2)}{}_2F_1\left(1+i\eta_i; -i\eta_f; 1; \frac{2(p_i p_f - p_i\cdot p_f)}{\gamma^2+\Delta^2}\right).$$

In these equations, S_i and S_f represent appropriate spectroscopic factors for the neutron states, and the Coulomb functions φ_i are normalized to asymptotic spherical waves. The initial and final c.m. wave numbers are k_i and k_f with M_i and M_f the appropriate reduced masses. The normalization constant C has the value $|C(\eta)|^2 = 2\pi\eta[\exp(2\pi\eta)-1]^{-1}$ (below the Coulomb barrier) and the Coulomb parameter η_i is given by $\eta_i = ZZ'e^2mM_i/\hbar^2k_i$. The quantity γ is the binding energy wave number and Δ the momentum transfer parameter $|p_i-p_f|$. The results of the cross-section calculation are shown in fig. 1 where they are compared with the experiment data of Kuhn and Schlenk [7]). The agreement between theory and experiment is good for energies up to 700 keV, but deteriorates in the vicinity of the Coulomb barrier. This is reasonable, because the assumptions made by May and Clayton [2]) breakdown in this region, and there is an increasing probability of alternative reaction mechanisms. The overall conclusion is therefore that not only is diproton production important below the Coulomb barrier but it is the dominant mechanism by which the reaction between two helions can proceed at such energies.

The effect of diproton production on the hydrogen burning cycle.

The results of an experiment recently reported by Slobodrian *et al.* [8]) suggest a cross section for the reaction $^3\text{He}+{}^3\text{He} \rightarrow {}^4\text{He}+e^+ +\nu$ at 13.6 MeV energy which is of the order of nb and greatly in excess of theoretical expectations. The authors

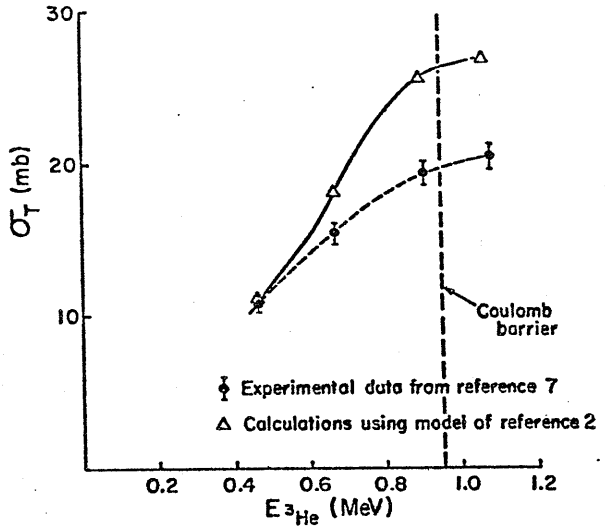

Fig. 1. Comparison of the predicted total reaction cross section from the neutron tunnelling model with experimental results for the reaction $^3He+^3H \rightarrow ^4He+^2H$.

could not determine whether this reaction proceeds by a direct mechanism or through an intermediate diproton state at this energy. The tunnelling calculation on the other hand has identified diproton production as the dominant channel by which the $^3He+^3He \rightarrow ^4He+2p$ reaction proceeds below the Coulomb barrier. It follows therefore that a diproton branch must necessarily be included in the hydrogen burning cycle (see fig. 2), since reaction energies are sufficiently low (typically 10 keV). If in addition, a rate for β-decay of the diproton consistent with ref. [8]) is included in the calculation of reaction rates for the various stages of the proton chain, it becomes possible to estimate the effect of diproton decay on energy production in the sun.

Standard stellar models for main sequence stars assume that hydrostatic equilibrium exists between the gravitional force and the pressure gradient; that energy is transported by radiation; and that the energy is produced in a hydrogen burning

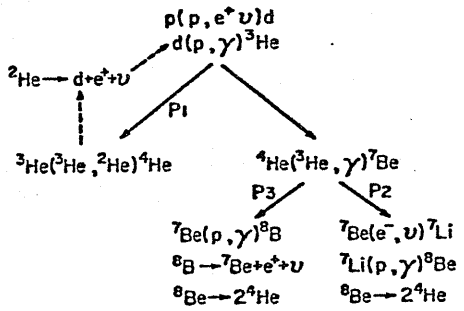

Fig. 2. Energy production in the hydrogen burning cycle.

cycle. Since the first results were obtained from the neutrino capture experiment by Davis *et al.* [9]), much effort has been put into bringing the predicted solar neutrino flux from these models into agreement with the observed value (the latest figure being 1.5 SNU). However to date neither further measurements of nuclear cross sections [10]) nor variations in the input parameters [11]) have overcome the discrepancy between theory and this experimental result. A review of the position prior to 1972 is given by Bahcall and Sears [12]).

We attempt in this paper to estimate the effect of diproton production and its β-decay on the proton chain using a standard solar model, and assuming an average equilibrium for the intermediate nuclei [see Schwarzschild [13]) and Iben [14])]. Inclusion of the β-decay of the diproton in the equilibrium equations gives

$$r_{11}+r_{33}^{d} = r_{12}, \tag{1}$$

$$r_{12} = 2r_{33}^{2p}+2r_{33}^{d}+r_{34}, \tag{2}$$

$$r_{34} = r_{17}+r_{7e^-}, \tag{3}$$

where r_{ij} denotes the reaction rate for particles i and j, r_{33}^{2p} denotes the reaction rate for ^{3}He(^{3}He, 2p)^{4}He, r_{33}^{d} denotes the reaction rate for ^{3}He(^{3}He, de$^+\nu$)^{4}He, and r_{7e^-} denotes the reaction rate for electron captive by ^{7}Be.

Eqs. (1) and (2) can be rewritten as

$$\frac{r_{11}}{r_{33}^{2p}} = 2+\frac{r_{33}^{d}}{r_{33}^{2p}}+\frac{r_{34}}{r_{33}^{2p}}.$$

This differs from previous equations only in the introduction of the term r_{33}^{d}/r_{33}^{2p}. The reaction rate r_{ij} can be written in the form

$$r_{ij} \propto \rho^2 X_i X_j \frac{S}{T^{\frac{2}{3}}} e^{-\beta T^{\frac{1}{3}}},$$

where ρ denotes the density of the sun's core, X_i and X_j the abundances by weight of reacting nuclei, and S is the astrophysical cross section factor, defined as

$$\sigma(E) = \frac{S}{E} e^{-2\pi\eta},$$

η being the Coulomb parameter, β a function of A and Z for the nuclei concerned, and T the temperature in degrees Kelvin. This ratio is simply that of the appropriate cross sections since all other terms cancel, and is therefore the branching ratio between the decay of the diproton by β-emission and by the strong decay ^{2}He$\rightarrow$p+p. Clearly the inclusion of the diproton and its β-decay in the hydrogen burning cycle will not significantly affect the present solar model nor contribute a solution to the solar neutrino problem.

References

1) R. J. Slobodrian, J. S. C. McKee, W. F. Tivol, D. J. Clark and T. A. Tombrello, Phys. Lett. 25B (1967) 19
2) R. M. May and D. D. Clayton, Astrophys. J. 153 (1968) 855
3) G. Breit and M. E. Ebel, Phys. Rev. 103 (1956) 679
4) M. R. Dwarakanath and H. Winkler, Phys. Rev. C4 (1971) 1532
5) W. J. Roberts, E. E. Gross and E. Newman, Phys. Rev. C9 (1974) 149
6) K. S. Nam, G. M. Osetinskii and V. A. Sergeev, Yad. Fiz. 10 (1969) 705
7) B. Kühn and B. Schlenk, Nucl. Phys. 48 (1963) 353
8) R. J. Slobodrian, R. Pigeon and M. Irshad, Phys. Rev. Lett. 35 (1975) 19
9) R. Davis, Jr., L. C. Rogers and V. Radika, Bull. Am. Phys. Soc. 16 (1971) 631
10) W. A. Fowler, G. R. Caughlan and B. A. Zimmerman, Ann. Rev. Astron. and Astrophys. 13 (1975) 69
11) I. Iben, Jr., Ann. of Phys. 54 (1969) 164
12) J. N. Bahcall and R. L. Sears, Ann. Rev. Astron. and Astrophys. 10 (1972) 25
13) M. Schwarzschild, Structure and evolution of the stars (Princeton University Press, 1958)
14) I. Iben, Jr., Astrophys. J. 141 (1965) 993

BIBLIOGRAPHY

Bang, J., J. M. Herman (1959) Mats.-Fys Medd 31 p. 13

Bambynek, W., B. Craseman, R. W. Fink, H. U. Freund, H. Mark, R. E. Price, P. V. Rao (1972) Rev. Mod. Phys. 44 p. 716

Batton, R. A., J. Bruckshaw, I. Gusdal, G. Knote, A. McIlwain, J. S. C. McKee, S. Oh (1976) to be published Nucl. Inst. Meth.

Beardon, J. A. (1967) Rev. Mod. Phys. 39 p. 78

Bissinger, G. A., S. M. Shafroth (1972) Phys. Rev. A5 p. 2046

Bodart, F., G. Deconninck, J. Hontoy, S. F. J. Wilk (1973) Radio Chem. Radioanal. Letters 13 p. 161

Bodart, F., S. F. J. Wilk, G. Deconninck (1975) X-Ray Spectrometry 4 p. 161

Camp, D. C., A. L. VanLehn, J. R. Rhodes, A. H. Pradzynski (1975) X-Ray Spectrometry 4 p. 123

Chadwick, J. (1912) Phil. Mag. 24 p. 594

Charpak, G. (1970) Annual Review of Nuclear Science 20 p. 195

Dyson, N. A. (1975) Phys. Med. Biol. 20 p. 1

Ebert, P. J., V. W. Slivinsky (1969) Phys. Rev. 188 p. 1

Folkmann, F., C. Gaarde, T. Huus, K. Kemp (1974) Nucl. Inst. Meth. 116 p. 487

Garcia, J. D. (1970) Phys. Rev. A1 p. 280, A1 p. 1402

Garcia, J. D., R. J. Fortner, T. M. Kavanagh (1973) Rev. Mod. Phys. 45 p. 111

Gordon, B. M., H. W. Kraner (1972) Journal of Radioanal. Chem. 12 p. 181

Gray, D. E. (1957) American Institute of Physics Handbook 5-48

Gryzinski, M. (1965) Phys. Rev. 138A p. 336

Hanson, J. S., H. U. Freund, R. W. Fink (1970) Nucl. Phys. A142 p. 604

Henneberg, W. (1933) Z. Physik. 86 p. 592

Herman, A. W., L. A. McNelles, J. L. Campbell (1973) Int. Journal App. Rad. Isotopes 24 p. 677

Johansson, T. B., R. Akselsson, S. A. E. Johansson (1970) Nucl. Inst. Meth. 84 p. 141

Kliwer, J. K., J. J. Kraushaar, R. A. Ristinen, H. Rudolph, W. R. Smythe (1972) Am. Phys. Soc. 17 p. 504

Kostroun, V. O., M. H. Chen, B. Crasemann (1971) Phys. Rev. A3 533; A4 p. 1

Lee, D. M., S. E. Sobottka, H. A. Thiessen (1972) Nucl. Inst. Meth. 104 p. 179

Lee, D. M., S. E. Sobottka, H. A. Thiessen (1973) Nucl. Inst. Meth. 109 p. 421

Lee, D. M., S. E. Sobottka, H. A. Thiessen (1974) Nucl. Inst. Meth. 120 p. 153

McGuire, E. J. (1969) Phys. Rev. 185 p. 1

Merzbacher, E., H. W. Lewis (1958) Handbuch der Physik (Springer-Verlag, Berlin) 34 p. 166

Middleman, L. M., R. L. Ford, R. Hofstadter (1970) Phys. Rev. A2 p. 1429

Nelson, G. C., B. G. Saunders (1969) Phys. Rev. 188 p. 108

"Nucleonics Data Sheet No. 1, Physical Constants" (1955) Nucleonics 13 p. 36

Palladino, V., B. Sadoulet (1974) LBL-3013 Lawrence Berkeley Laboratory

Pogson, R. H. (1976) Master's Thesis, University of Manitoba

Rao, P. V., M. H. Chen, B. Crasemann (1972) Phys. Rev. A5 p. 997

Scofield, J. H. (1969) Phys. Rev. 179 p. 9

Slivinsky, V. W., P. J. Ebert (1969) Phys. Lett. 29A p. 463

Slobodrian, R. J., R. Pigeon, M. Irshad (1975) Phys. Rev. Lett. 35 p. 19

Stetz, A. W., V. Perez-Mendez (1973) LBL-2064 Lawrence Berkeley Laboratory

Teoh, W. (1973) Nucl. Inst. Meth. 109 p. 509

Verba, J. W. (1972) Journal of Radioanal. Chem. 12 p. 181

Walter, R. L., R. D. Willis, W. F. Gutkneckt, J. M. Joyce (1972) Ad. in X-Ray Anal. 15 p. 373

Walters, D. L., C. P. Bahalla (1971) Phys. Rev. A3 p. 519; A4 p. 2164

Watkins, D. A. (1958) "Topics in Electromagnetic Theory" (J. Wiley, New York)

APPENDIX I

1. X-ray and Gamma ray Interactions with Matter

There are three competing processes by which high energy photons can lose energy in passing through matter. These are:

The Photoelectric Effect. The photon is annihilated through interaction with an atomic electron, the latter gaining enough energy to escape from the atomic levels.

Compton Scattering. The photon undergoes an inelastic collision with one atomic electron. This again causes the ionization of the atom, however the photon is not annihilated, its energy is only reduced.

Pair Production. The photon interacts with the nuclear Coulombic force, this perturbation causing the photon to split into an electron-positron pair. The threshold photon energy for this process being the energy equivalent of the rest mass of the pair ie. 1.02 MeV.

These processes are shown schematically in Fig. 1 taken from Enge, Wehr and Richards - Introduction to Atomic Physics p. 296. Fig. 2, from the same page, demonstrates the energy dependence of these phenomena with respect to photon energy.

2. Compton Background in Solid State Detectors

Gamma rays hitting the detector crystal lose energy through one of these processes. If the second occurs, then there is the possibility that the gamma ray after Compton scattering leaves the detector without losing all its energy. This will result in a pulse which does not correspond to the true energy of the gamma ray but to a photon of lower energy. Thus the flux of gamma rays from nuclear reactions in the target will produce a Compton background component in the energy region

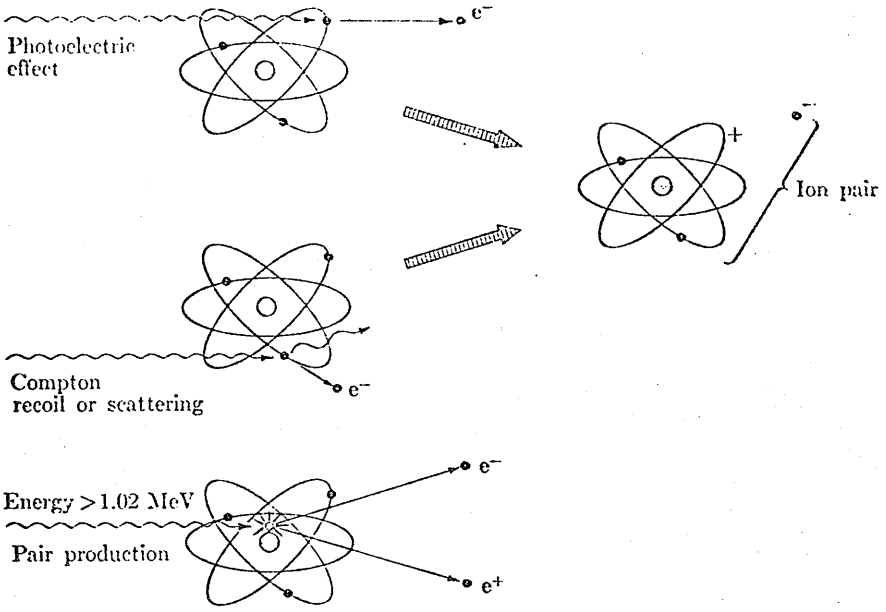

Figure 1. Summary of x-ray and gamma-ray interactions with matter.

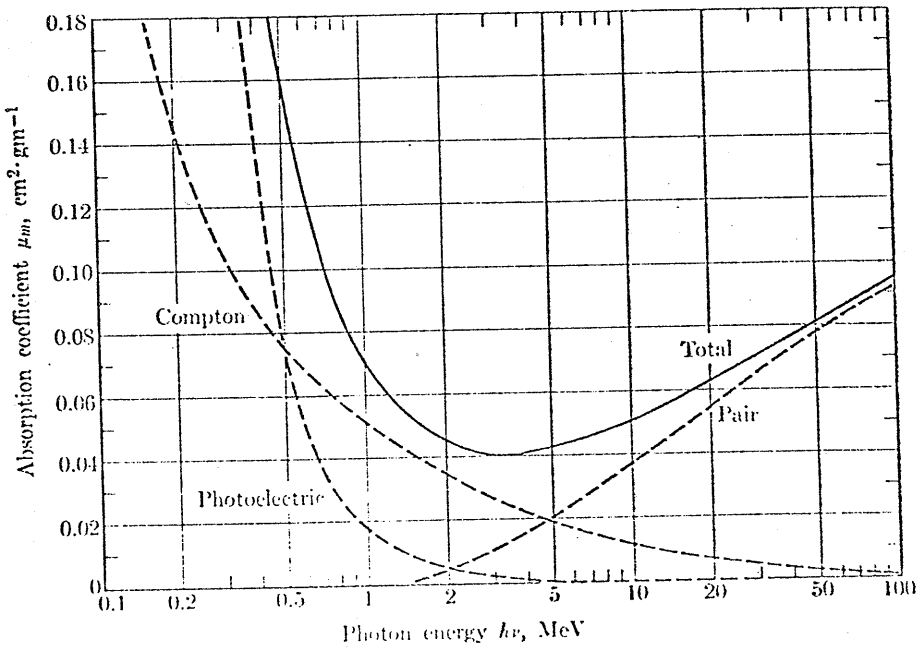

Figure 2. Total mass-absorption coefficients for gamma rays in lead and the contributions from the photoelectric effect, the Compton effect, and pair production.

associated with X-ray energies. Since the cross sections for gamma emitting nuclear reactions increase substantially from 3 to 40 MeV. A corresponding increase in X-ray background would be expected.

APPENDIX II

The programs used in the design of the magnetic regenerator:

1. Field mapping and proton deflection
2. Orbit deflection
3. Subprogram: LINE
4. Subprogram: LINE2
5. Subprogram: MAGFLD
6. Subprogram: INTGRL

1. Field Mapping and Proton Deflection

```
LEVEL 21.7 ( JAN 73 )                                   CS/360  FORTRAN H

          COMPILER OPTIONS - NAME=  MAIN,OPT=02,LINECNT=65,SIZE=0000K,
                             SOURCE,EBCDIC,NOLIST,NODECK,LOAD,MAP,NOEDIT,ID,NOXREF

ISN 0002                    IMPLICIT REAL*8 (A-H,O-Z)
ISN 0003                    DIMENSION BB(150), BBA(70), Z1(150)
ISN 0004                    EQUIVALENCE (BB(1),BBA(1))
ISN 0005          302       FORMAT (1H ,4X,F6.4,4X,F14.9,4X,F14.9,4X,I3,4X,I3//)
ISN 0006          303       FORMAT ((10(2X,E10.3))//)
ISN 0007                    PI=3.14159265358979 32
ISN 0008                    CONV=180./PI
ISN 0009                    R=-2.6
ISN 0010                    R=0.5
ISN 0011                    DO 300 J=1,51
ISN 0012                    DO 200 II=1,150
ISN 0013                    BB(II)=0.0
ISN 0014          200       CONTINUE
ISN 0015                    Y=-0.05+0.001*(J-1)
ISN 0016                    R1=R+Y
ISN 0017                    DO 301 K=1,101
ISN 0018                    X=-0.05+0.001*(K-1)
ISN 0019                    Z1(K)=DSQRT(X**2+Y**2)
ISN 0020                    IF (X.LT.0.0) Z1(K)=-Z1(K)
ISN 0022                    IF (Z1(K).GT.0.05) GO TO 131
ISN 0024                    IF (Z1(K).LE.-0.05) N=K
ISN 0026          301       CONTINUE
ISN 0027          131       M=K
ISN 0028                    S=0.005
ISN 0029                    CALL MAGFLD(N,M,S,Z1,BE)
ISN 0030                    P=0.018
ISN 0031                    S=0.0025
ISN 0032                    CALL LINE(N,M,S,Y,P,BB)
ISN 0033                    P=0.035
ISN 0034                    S=0.002
ISN 0035                    CALL LINE(N,M,S,Y,P,BB)
ISN 0036                    I=N+1
ISN 0037                    CALL INTGRL(I,M,R1,BE,TAREA,THI)
ISN 0038                    THID=THI*CONV
ISN 0039                    WRITE (6,302) Y,TAREA,THID,N,M
ISN 0040                    IF (J/10*10.NE.J) GO TO 300
ISN 0042                    WRITE (6,303) BBA
ISN 0043          300       CONTINUE
ISN 0044                    STOP
ISN 0045                    END
```

2. Orbit Calculation

```
LEVEL 2.1  ( JAN 75 )                          OS/360  FORTRAN H EXTENDED              DATE 76.062/15.45.37

REQUESTED OPTIONS: ,EB,,,,OBJ,,MAP,,GOSTMT,,,S,NAME(MAIN),OPT(0),LC(654),AD(NONE),FLAG(I),

OPTIONS IN EFFECT: NAME(MAIN) NOOPTIMIZE LINECOUNT(654) SIZE(MAX) AUTODBL(NONE)
                   SOURCE EBCDIC NOLIST NODECK OBJECT MAP NOFORMAT GOSTMT NOXREF NOALC NOANSF

                C
                C
                C     ORBIT .... THIS PROGRAM CALCULATES THE PATH OF THE PROTONS IN THE
                C     OUTER REGION OF THE CYCLOTRON WHEN  A PEELER AND MAGNETIC REGENERATOR
                C     ARE INCLUDED. THE PURPOSE IS TO INCREASE THE SEPARATION OF THE ORBITS AT
                C     ONE POINT SUFFICIENTLY TO MAKE POSSIBLE THE EXTRACTION OF BEAM USING
                C     AN ELECTROSTATIC DEFLECTOR
                C
                C
                C     BA    .. THE AVERAGE MAG FIELD
                C     R     .. THE RADIUS AT WHICH THE RAGENERATOR POSITIONED
                C     R1    .. THE RADIUS OF PROTON ORBIT (THE CYCLOTRON FIELD IS APPROXIMATED
                C             BY A MEAN FIELD .. BA
                C     SEP   .. THE SEPARATION BETWEEN CONSECUTIVE ORBITS
                C     YIN   .. DISTANCE OF ORBIT INTERSECTION ON AXIS TO CENTRE REGENERATOR
                C     B1A   .. ENTRANCE ANGLE OF PROTON ORBIT INTO THE REGENERATOR
                C     A1A   .. EXIT ANGLE OF PROTON ORBIT FROM REGENERATOR
                C     YMIN  .. DISTANCE ALONG Y AXIS TO X AXIS OF THE RFGENERATOR AT EDGE OF
                C             ITS EFFECTIVE FIELD
                C     P . S .. DEFINE THE POSITION AND RADIUS OF THE SPHERES WHICH MAKE UP
                C     THE REGENERATOR
                C     (XCEN,YCEN) & (XC,YC) ARE THE PRESENT AND PREVIOUS CENTRE OF ORBIT
                C
                C
                C
ISN 0002              IMPLICIT REAL*8 (A-H,O-Z)
ISN 0003              DIMENSION Z1(150), BB(150)
ISN 0004              PI=3.1415926535897932
ISN 0005              CONV=180./PI
ISN 0006              R=0.5664
ISN 0007              RINC=0.0002
ISN 0008              R1=R-0.05
ISN 0009              R2=R1
ISN 0010              XC=0.0
ISN 0011              YC=0.0
ISN 0012              YIN=0.05
ISN 0013              B1A=0.0
ISN 0014              C=1.043E-8
ISN 0015              CR=9.588E7
ISN 0016              DAX=15.*PI/180.
ISN 0017              DMIN=0.565
ISN 0018              WRITE (6,610)
ISN 0019              J=0
ISN 0020        120   CONTINUE
ISN 0021              J=J+1
```

```
ISN  0022              DO 200 II=1,150
ISN  0023              BB(II)=0.0
ISN  0024      200     CONTINUE
ISN  0025              ORBIT=((J+1)/2)*1.0
ISN  0026              Q=(-1)**(J+1)
ISN  0027              YMIN=-Q*(0.05*DTAN(B1A))+YIN
ISN  0028              DO 301 K=1,102
ISN  0029              Y=YMIN+(K-1)*Q*0.001*DSIN(B1A)
ISN  0030              X=-0.05+(K-1)*0.001*DCOS(B1A)
ISN  0031              Z1(K)=DSQRT(X**2+Y**2)
ISN  0033              IF (X.LT.0.0) Z1(K)=-Z1(K)
ISN  0035              IF (Z1(K).GT.0.05) GO TO 131
ISN  0037              IF (Z1(K).LE.-0.05) N=K
ISN  0039      301     CONTINUE
ISN  0040      131     M=K
ISN  0041              S=0.005
ISN  0042              CALL MAGFLD(N,M,S,Z1,BB)
ISN  0043              P=0.019
ISN  0044              S=0.00235
ISN  0045              CALL LINE2(N,M,S,P,YMIN,B1A,BB)
ISN  0046              P=0.029
ISN  0047              S=0.0019
ISN  0048              CALL LINE2(N,M,S,P,YMIN,B1A,BB)
ISN  0049              S=0.0018
ISN  0050              P=0.04
ISN  0051              CALL LINE2(N,M,S,P,YMIN,B1A,BB)
ISN  0052              I=N+1
                C
                CCCCCC
                CCCCCC INTEGRATES THE MAGNETIC FIELD BETWEEN THE POINTS WHERE THE PROTONS
                CCCCCC ENTER AND LEAVE THE REGENERATOR AND CALCULATES THE RESULTING DEFLECTION
                CCCCCC ASSUMING A STRAIGHT PATH
                CCCCCC BA  .. THE AVERAGE MAGNETIC FIELD
                CCCCCC V   .. TANGENTIAL VELOCITY COMPONENT OF ORBIT
                CCCCCC VEL .. RADIAL VELOCITY COMPONENT OF ORBIT
                CCCCCC
                C
ISN  0053              TAREA=0.0
ISN  0054              DO 137 K=I,M
ISN  0055              AREA=((BB(K-1)+BB(K))/2)*0.001
ISN  0056              TAREA=AREA+TAREA
ISN  0057      137     CONTINUE
ISN  0058              IF (R2.GE.0.5588) GO TO 165
ISN  0060              BA=(R2-0.5156)*0.111-2.018
ISN  0061              GO TO 166
ISN  0062      165     BA=(R2-0.5588)*0.128-1.97
ISN  0063      166     CONTINUE
ISN  0064              V=BA*R1
ISN  0065              VEL=TAREA
ISN  0066              THI=2*DARSIN(VEL*0.5/V)
ISN  0067              A1A=B1A+THI
ISN  0068              A1AD=A1A*CONV
```

```
C
C
C     CALCULATION OF THE CENTRE OF THE ORBIT BETWEEN PEELER AND REGENERATOR
C     AND THE SEPRATION OF THE ORBITS AT THE POINT IN THE PATH AT 45. TO
C     THE PEELER AND REGENERATOR
C     CALCULATE THE INTERSECTION OF THE PRPTON ORBIT AT THE NEXT AXIS
C     R2 IS THE DISTANCE FROM THE CENTRE OF THE CYCLOTRON TO THIS INTERSECTION
C     AND YIN IS THE DISTANCE FROM THE CENTRE OF THE REGENERATOR TO INTERSECTION
C
ISN 0069            IF (J/2*2.EQ.J) GO TO 141
ISN 0071            XCEN=R1*DSIN(A1A)
ISN 0072            YCEN=R2-R1*DCOS(A1A)
ISN 0073            XSEP=XCEN-XC
ISN 0074            YSEP=YCEN-YC
ISN 0075            SEP=DSQRT(XSEP**2+YSEP**2)
ISN 0076            IF (XSEP.LT.0.0) SEP=-SEP
ISN 0078            XC=XCEN
ISN 0079            YC=YCEN
ISN 0080            B1A=DARSIN(YCEN/R1)
ISN 0081            R2=R1*DCOS(B1A)+XCEN
ISN 0082            GO TO 144
ISN 0083      141   CONTINUE
ISN 0084            XCEN=R2-R1*DCOS(A1A)

ISN 0085            YCEN=R1*DSIN(A1A)
ISN 0086            SEP=0.0
ISN 0087            R1=R1+RINC
ISN 0088            B1A=DARSIN(XCEN/R1)
ISN 0089            R2=R1*DCOS(B1A)+YCEN
ISN 0090      144   CONTINUE
ISN 0091            YIN=R2-R
ISN 0092            IF (R2.GT.R3) GO TO 145
ISN 0094            WRITE (6,611) ORBIT,A1AD,XCEN,YCEN,SEP,N,M,B1A
ISN 0095            GO TO 120
ISN 0096      145   CONTINUE
ISN 0097            STOP
ISN 0098            END
```

3. Subprogram LINE

```
        COMPILER OPTIONS - NAME=  MAIN,OPT=02,LINECNT=65,SIZE=0000K,
                           SOURCE,EBCDIC,NOLIST,NODECK,LOAD,MAP,NOEDIT,ID,NOXREF
ISN 0002                SUBROUTINE LINE(N,M,S,Y,P,BB)
ISN 0003                IMPLICIT REAL*8 (A-H,O-Z)
ISN 0004                DIMENSION Z1(150),  BB(150)
ISN 0005                YY=Y+P
ISN 0006                DO 1 K=N,M
ISN 0007                X=-0.05+0.001*(K-1)
ISN 0008                Z1(K)=DSQRT(X**2+YY**2)
ISN 0009      1         CONTINUE
ISN 0010                CALL MAGFLD(N,M,S,Z1,BB)
ISN 0011                RETURN
ISN 0012                END
```

4. Subprogram LINE2

```
OPTIONS IN EFFECT: NAME(MAIN) NOOPTIMIZE LINECOUNT(654) SIZE(MAX) AUTODBL(NONE)
                   SOURCE EBCDIC NOLIST NODECK OBJECT MAP NOFORMAT GOSTMT NOXREF NOALC NOANSF

ISN 0002                SUBROUTINE LINE2(N,M,S,P,YMIN,B1A,BB)
                  C
                  C     LINE2 .... THIS CALCULATES THE COORDINATES OF THE PROTON PATH WITHIN
                  C     THE REGENERATOR
                  C
                  C     (SHOULD ONLY BE USED WITH ORBITS PROGRAM)
                  C
ISN 0003                IMPLICIT REAL*8 (A-H,O-Z)
ISN 0004                DIMENSION Z1(150), BB(150)
ISN 0005                YY=P+YMIN
ISN 0006                DO 2 K=N,M
ISN 0007                X=-0.05+(K-1)*0.001*DCOS(B1A)
ISN 0008                Y=YY+(K-1)*0.001*DSIN(B1A)
ISN 0009                Z1(K)=DSQRT(X**2+Y**2)
ISN 0010              2 CONTINUE
ISN 0011                CALL MAGFLD(N,M,S,Z1,BB)
ISN 0012                RETURN
ISN 0013                END
```

5. Subprogram MAGFLD

```
ISN 0002              SUBROUTINE MAGFLD(N,M,S,Z1,BB)
                C
                C
                C     CALCULATES THE MAGNETIC FIELD  ALONG THE PATH OF THE PROTONS DUE TO
                C     REGENERATOR AND ADDS THIS TO THE FIELDS OF ADJACENT SPHERES
                C
                C
                C     B     .. MAGNETIC FIELD AT THE REGENERATOR
                C     PERM  .. PERMEABILITY OF THE MAGNETIC POLES
                C     W     .. DISTANCE CENTRE REGENERATOR TO EDGE OF THE POLES
                C     V     .. DISTANCE CENTRAL PLANE OF CYCLOTRON TO EDGE OF POLES
                C     SUS   .. SUSCEPTIBILITY OF REGENERATOR
                C     MAGM  .. MAGNETIC MOMENT INDUCED IN THE REGENERATOR BY THE POLES ASSUMING
                C              THE SPHERES BEHAVE AS SIMPLE DIPOLES
                C     BRAD  .. THE RADIIAL COMPONENT OF THE DIPOLE FIELD OF THE REGENERATOR
                C     BANG  .. THE TANGENTIAL COMPONENT OF THE DIPOLE FIELD OF THE REGENERATOR
                C     BB    .. THIS ARRAY CONTAINS THE MAGNETIC FIELD OF THE REGENERATOR
                C              AT ALL POINTS ALONG THE PROTON PATH PRESENTLY BEING CONSIDERED
                C              THIS IS DONE BY CALCULATING THE VERTICAL COMPONENT OF EACH
                C              SPHERE AT THE POINTS IN THE CENTRAL PLANE OF THE CYCLOTRON
                C              DOUBLING THIS GIVES THE THE TOTAL FIELD. COMPONENTS FROM
                C              PREVIOUSLY CONSIDERED SETS OF SPHERES ARE THEN ADDED
                C
                C
ISN 0003              IMPLICIT REAL*8 (A-H,O-Z)
ISN 0004              REAL*8 MAGM

ISN 0005              DIMENSION Z1(150),BB(150)
ISN 0006              B=-2.5
ISN 0007              W=0.012
ISN 0008              V=0.019
ISN 0009              PERM=1.8
ISN 0010              SUS=2.0
ISN 0011              PI=3.1415926535897932
ISN 0012              U0=12.5664E-7
ISN 0013              MAGM=4.*(-1)*PI*S**3*SUS*B/(U0*3.)
ISN 0014              CON=MAGM*U0/(4*PI)
ISN 0015              DO 135 K=N,M
ISN 0016              Z2=DABS(Z1(K))
ISN 0017              BYTOT=0.0
ISN 0018              L=1
ISN 0019              Q=V*(L/2*2)-W*(-1)**L
ISN 0020              Z=DSQRT(Z1(K)**2+Q**2)
ISN 0021              THETA=DATAN(Z2/Q)
ISN 0022              F=((PERM-1)/(PERM+1))**(L/2)
ISN 0023              T=0.
ISN 0024              IF (L/2*2.EQ.L) T=PI
ISN 0026              THETA=T+THETA*(-1)**((L+3)/2)
ISN 0027              BRAD=CON*2*F*DCOS(THETA)/(Z**3)
ISN 0028              BANG=CON*F*DSIN(THETA)/(Z**3)
ISN 0029              BY=(BRAD*DCOS(THETA)-BANG*DSIN(THETA))*(-1)**((L+2)/2)
ISN 0030              BYTOT=BY+BYTOT
ISN 0031        136   CONTINUE
ISN 0032              BB(K)=2*BYTOT+BB(K)
ISN 0033        135   CONTINUE
ISN 0034              RETURN
ISN 0035              END
```

6. Subprogram INTGRL

```
LEVEL 21.7 ( JAN 73 )                          OS/360  FORTRAN H

          COMPILER OPTIONS - NAME=  MAIN,OPT=02,LINECNT=65,SIZE=0000K,
                             SOURCE,EBCDIC,NOLIST,NODECK,LOAD,MAP,NOEDIT,ID,NOXREF
  ISN 0002              SUBROUTINE INTGRL(I,M,R1,BB,TAREA,THI)
                    C
                    C
                    C     INTEGRATES THE MAGNETIC FIELD BETWEEN THE POINTS WHERE THE PROTONS
                    C     ENTER AND LEAVE THE REGENERATOR AND CALCULATES THE RESULTING DEFLECTION
                    C     ASSUMING A STRAIGHT PATH
                    C
                    C
  ISN 0003              IMPLICIT REAL*8 (A-H,O-Z)
  ISN 0004              DIMENSION BB(150)
  ISN 0005              TAREA=0.0
  ISN 0006              B=-2.6
  ISN 0007              DO 137 K=I,M
  ISN 0008              AREA=((BB(K-1)+BB(K))/2)*0.001
  ISN 0009              TAREA=AREA+TAREA
  ISN 0010       137    CONTINUE
  ISN 0011              VEL=TAREA
  ISN 0012              V=B*R1
  ISN 0013              THI=DATAN(VEL/V)
  ISN 0014              RETURN
  ISN 0015              END
```